

Corotating Clumps Around Adolescent Low-Mass Stars: Four Years of Complex Quasiperiodic Variables from TESS

—AUTHOR LIST & ORDER NOT FINAL,¹ LUKE G. BOUMA,^{1,*} RAHUL JAYARAMAN,² SAUL RAPPAPORT,² LUISA M. REBULL,¹ ALEXANDRE DAVID-URAZ,^{3,4} LYNNE A. HILLENBRAND,¹ GÁSPÁR Á. BAKOS,⁵
—SUGGESTED CONTRIBUTORS, PENDING DISCUSSION, COMMENTS, ANALYSES, ETC—⁶,
MAXIMILIAN N. GÜNTHER,⁶ GEORGE R. RICKER,² AND JOSHUA N. WINN⁵

¹Department of Astronomy, MC 249-17, California Institute of Technology, Pasadena, CA 91125, USA

²MIT Kavli Institute and Department of Physics, 77 Massachusetts Avenue, Cambridge, MA 02139

³Department of Physics and Astronomy, Howard University, Washington DC, 20059

⁴Center for Research and Exploration in Space Science and Technology, and X-ray Astrophysics Laboratory, NASA/GSFC, Greenbelt, MD 20771, USA

⁵Department of Astrophysical Sciences, Princeton University, 4 Ivy Lane, Princeton, NJ 08540, USA

⁶European Space Agency (ESA), European Space Research and Technology Centre (ESTEC), Keplerlaan 1, 2201 AZ Noordwijk, Netherlands

(Received —; Revised —; Accepted —)

ABSTRACT

Complex quasiperiodic variables (CQVs) are low-mass pre-main-sequence stars with nearly periodic optical modulation. The modulation is likely induced by dust or gas clumps in orbit at the Keplerian corotation radius. Here, we report new CQVs discovered in TESS short-cadence data collected between July 2018 and Sep 2022. Our search of 65,760 K and M dwarfs with $T < 16$ and $d < 150$ pc yielded 53 high-quality CQVs. Most of these discoveries are new, and they include the brightest ($T \approx 9.5$), closest ($d \approx 20$ pc), and oldest (≈ 200 Myr) examples of this class of object currently known. A few objects are outliers: LP 12-502 for instance showed a “dip complex” with a period and duration that were fixed over 1,500 cycles, but in detail, this system exhibited between four and eight local minima per cycle, and at times also displayed multiple periods simultaneously. We demonstrate that transient corotating material is the most viable explanation for this class of object, and present evidence supporting the hypothesis that this material is sculpted by stellar magnetic fields dominated by high order multipoles. We expect that our sample will facilitate future efforts aimed at connecting CQVs to the broader contexts of star, disk, and perhaps even exoplanet evolution.

Keywords: Weak-line T Tauri stars (1795), Periodic variable stars (1213), Circumstellar matter (241), Star clusters (1567), Stellar magnetic fields (1610), Stellar rotation (1629)

1. INTRODUCTION

All pre-main-sequence stars vary in optical brightness, and the origin of such variability is, in most cases, understood. Well-explored sources of optical variability include inhomogeneities on stellar surfaces such as starspots and faculae (e.g. Basri 2021), occultations by gas-rich circumstellar disks (e.g. Bodman et al. 2017), and, in geometrically favorable circumstances, eclipses by stars and planets (e.g. Winn 2010). More exotic forms of optical variability relevant to this work include transiting exocomets (e.g. β Pic; Zieba et al. 2019) and disintegrating rocky bodies around both M dwarfs (e.g. KOI-2700; Rappaport et al. 2014) and white dwarfs (e.g. WD 1145; Vanderburg et al. 2015).

Corresponding author: Luke G. Bouma
luke@astro.caltech.edu

* 51 Pegasi b Fellow

Data from K2 and TESS have yielded a new class of variable star whose root cause is only beginning to become clear: complex quasiperiodic variables (CQVs). These objects are identified from their optical light curves, which show nearly periodic troughs that are either sharp or broad; these troughs are often superposed on smooth spot-like modulation (Stauffer et al. 2017, 2018; Zhan et al. 2019). Some CQVs show up to eight local minima (“dips”) per cycle. Most are pre-main-sequence M dwarfs without near-infrared excesses, ages of $\approx 5\text{--}150$ million years (Myr), and rotation periods of at most two days; they are observed to comprise $\approx 1\text{--}3\%$ of M dwarfs younger than 100 Myr (Rebull et al. 2016; Günther et al. 2022). The dips can be chromatic, with a reddening law plausibly consistent with dust (Onitsuka et al. 2017; Bouma et al. 2020; Günther et al. 2022; Koen 2023). And finally, while the dip shapes can “jump” between different depths and durations over less than one cycle, they more often evolve gradually, over tens to hundreds of cycles (e.g. Stauffer et al. 2017; Palumbo et al. 2022; Popinchalk et al. 2023).

The CQV light curves cannot be explained by pure starspots. Although all young M dwarfs are spotted, this tends to produce flux variations over characteristic timescales of the rotation period, P_{rot} , and its half-harmonic, $0.5P_{\text{rot}}$. If one fine-tunes the viewing geometry, starspots can produce dips with durations as short as $\approx 0.2P_{\text{rot}}$, and the dip amplitudes quickly decrease due to limb-darkening (see Stauffer et al. 2017, Figures 37-41). The observed dips can happen over durations as short as $0.05P_{\text{rot}}$ with characteristic depths of a few percent; a “starspot-only” scenario can be discarded for any object with dips that are sufficiently deep and short in duration (Stauffer et al. 2017; Koen 2021). The timescales and amplitudes of the flux variations in such objects instead require sharp geometries with material extrinsic to the stellar surface (e.g. Stauffer et al. 2017; Günther et al. 2022). Since the CQVs are probably all explained by the same phenomenon, we therefore discard the “spot-only” scenario.

A few competing explanations for what causes the complex quasiperiodic variability are shown in Figure 1. The “clump” scenario invokes opaque dust clumps periodically transiting the star near the Keplerian corotation radius, $R_{\text{cr}} = (GM/\Omega^2)^{1/3}$ (Stauffer et al. 2017; Sanderson et al. 2023). The “prominence” scenario invokes long-lived condensations of cool and dense marginally-ionized gas, embedded within the hotter corona, that would be centrifugally supported to also be near corotation (Collier Cameron & Robinson 1989; Jardine & Collier Cameron 2019; Waugh & Jardine 2022). Such structures are analogous to quiescent prominences and filaments seen in the solar corona (see e.g. Vial & Engvold 2015), though at much larger relative distances from the stellar surface. A final possibility is one of a “screen”, in which the inner wall of a quiescent circumstellar disk blocks a portion of the stellar surface to produce sudden dips whenever spots come into view (Zhan et al. 2019).

The dust clump and prominence hypotheses seem most plausible. They are qualitatively similar, except that one invokes opacity from dust, while the other invokes opacity from gas, likely bound-free transitions in hydrogen or perhaps a molecular opacity. The screen scenario seems inconsistent with the sharpness of the observed dips, the lack of infrared excess, and the observed lifetime of CQVs extending an order of magnitude longer than the $\approx 10^7$ year timescale often quoted for primordial disk dispersal. However, unambiguous evidence in support of any one scenario has yet to be acquired. Such evidence might include a spectroscopic detection of silicate $10\mu\text{m}$ dust absorption during a dip, or perhaps detection of transient Balmer-line excesses as a function of cycle phase, similar to observations made in systems such as AB Dor (see Collier Cameron 1999) or PTFO 8-8695 (Johns-Krull et al. 2016).

CQVs remain mysterious because they have been both hard to discover and hard to characterize. Discoverability is tied to rarity: CQVs comprise $\approx 1\%$ of the youngest $\approx 1\%$ of M dwarfs (Rebull et al. 2018). Out of the millions of stars monitored by K2 and TESS, about 50 CQVs have been reported to date (Rebull et al. 2016; Stauffer et al. 2017, 2018; Zhan et al. 2019; Bouma et al. 2020; Günther et al.

2022; Popinchalk et al. 2023). The known CQVs are correspondingly faint; the initial K2 discoveries (Rebull et al. 2016; Stauffer et al. 2017) were M2-M6 dwarfs at distances $\gtrsim 100\text{ pc}$, yielding optical brightnesses of $V \approx 15.5$ to $V > 20$. This renders time-series spectroscopy at high resolution out of reach for current facilities, despite its potential utility in ruling out some of these models.

In this work, we aim to find bright and nearby CQVs, since these objects will be the most amenable to detailed photometric and spectroscopic analyses. To do this, we use 120-second cadence data acquired by TESS between July 2018 and Sep 2022 (Sectors 1-55; Cycles 1-4). We present our search methods in Section 2, and the properties of the resulting CQV catalog in Section 3. The evolution of many CQVs over a two-year baseline is described in Section 4, including a deep-dive into LP 12-502. We discuss a few implications in Section 5, and conclude in Section 6.

A point on nomenclature. CQVs have been called “transient flux dips”, “persistent flux dips”, “scallop shells”, “batwings”, (Stauffer et al. 2017) “complex rotators”, (Zhan et al. 2019; Günther et al. 2022; Popinchalk et al. 2023) and “complex periodic variables” (Koen 2023). The CQVs should not be conflated with “dippers”, which are classical T Tauri stars with infrared excesses, and which show large-amplitude variability linked to obscuring inner disk structures and accretion hot spots (Cody et al. 2014; Robinson et al. 2021). While a few similarities between CQVs and dippers do exist (see Sections 3.3 and 5.7), their phenomenology and stellar properties are quite different. At the risk of introducing yet another standard, we hope to use a nomenclature that reflects how, when observed over timescales of more than tens of cycles, CQVs are almost but not exactly periodic. They are quasiperiodic. While the three-type classification scheme proposed by Stauffer et al. (2017) may indeed provide some helpful visual distinctions amongst the CQVs, it seems likely that they are all explained by a single underlying phenomenon, and so we opt to refer to them by a single empirically descriptive name. We also considered names that focused on the presence of transient corotating clumps, or more generally on circumstellar plasma tori; for the time being, “CQV” seems to more accurately mirror the state of our ignorance.

2. METHODS

2.1. Stellar selection function

We analyzed the “short” 120-second cadence data acquired by TESS between July 2018 and Sep 2022 (Sectors 1-55). Specifically, we used the 120-second cadence light curves produced by the Science Processing and Operations Center at NASA Ames (Jenkins et al. 2016). While the TESS data products from these sectors also included full frame images with cadences of 600 and 1800 seconds, we limited our scope in this study for the sake of simplicity in data handling. In exchange, we sacrificed both completeness and homogeneity of the selection function. While TESS cumulatively observed $\approx 90\%$ of the sky for at least one lunar month between July 2018 and Sep 2022, the 120-second cadence data were



Figure 1. Complex quasiperiodic variables (CQVs): *Top:* Phase-folded TESS light curves of three CQVs. Each is stacked over one month. Gray circles are raw 2-minute data; black circles bin to 300 points per cycle. Periods in hours are in the bottom right of each panel. Left-to-right, the objects are LP 12-502 (TIC 402980664; Sector 19), TIC 94088626 (Sector 10), and TIC 425933644 (Sector 28). *Bottom:* Cartoon explanations for the phenomenon. The dust clump scenario (lower left) and prominence scenario (lower center) both invoke centrifugally-supported material at the corotation radius. We disfavor the screen scenario (see Section 1).

collected for only a subset of observable stars during this time due to telemetric constraints (see Fausnaugh et al. 2021).

To assess the completeness of the resulting 120-second cadence data that is the basis of this study, we cross-matched TIC8 (Stassun et al. 2018) against the Gaia DR2 point-source catalog (Gaia Collaboration et al. 2018). We opted for Gaia DR2 rather than DR3 because the base catalog for TIC8 was Gaia DR2, which facilitated a one-to-one crossmatch using the Gaia source identifiers. This exercise showed that for $T < 16$ M dwarfs, the TESS 2-minute data are $\approx 50\%$ complete at ≈ 50 pc. At < 20 pc, $\gtrsim 80\%$ of the $T < 16$ M dwarfs have at least one sector of short-cadence data; at > 100 pc, $\lesssim 10\%$ of such M dwarfs have at least one sector of short-cadence data. Armed with this understanding, we then used our cross-match between Gaia DR2 and TIC8 to select our stars of interest, which we defined as stars with 120-second cadence TESS light curves that satisfied

$$T < 16 \quad (\text{Bright for TESS}) \quad (1)$$

$$G_{\text{BP}} - G_{\text{RP}} > 1.5 \quad (\text{Red stars only}) \quad (2)$$

$$M_{\text{G}} > 4 \quad (\text{Dwarf stars only}) \quad (3)$$

$$d < 150 \text{ pc} \quad (\text{Close stars only}), \quad (4)$$

for $M_{\text{G}} = G + 5 \log(\varpi_{\text{as}}) + 5$ the Gaia G -band absolute magnitude, ϖ_{as} the parallax in units of arcseconds, and a geometric distance d defined by inverting the parallax and ignoring any zero-point correction. The target sample therefore includes 65,760 M dwarfs and late-K dwarfs, down to $T < 16$ and out to $d < 150$ pc.

2.2. CQV discovery

Previous methods for finding CQVs have included visually examining stars known to be in young clusters (Rebull et al. 2016; Stauffer et al. 2017), and automatically flagging rapid rotators with a large number of strong Fourier harmonics (Zhan et al. 2019). The latter approach still requires visual vetting, since “stars with many Fourier harmonics” is a designation that includes objects such as eclipsing binaries or multiple stars blended into a single photometric aperture. In this work, we implemented a new search approach based on counting the number of sharp local minima in phase-folded light curves, while also using the previously tested Fourier approach. We applied these two search techniques independently.

2.2.1. Counting dips

The dip counting technique aims to count sharp local minima in phase-folded light curves. CQVs will preferably have at least three such minima in order to be distinct from false positives such as synchronized and spotted binaries (“RS CVn” stars).

For our dip-counting pipeline, we began with the PDC_SAP flux for each sector, removed non-zero quality flags, and normalized the light curve to one by dividing out its median value. We then flattened the light curve using a 5-day sliding median filter, as implemented in `wotan` (Hippke et al. 2019). On the resulting cleaned and flattened light curve, we ran a periodogram search, opting for the Stellingwerf (1978) phase dispersion minimization (PDM) algorithm implemented in `astrobase` (Bhatti et al. 2021) due to its shape agnosticism. If a period below 2 days was identified,

we reran the periodogram at a finer grid to improve the accuracy of the period determination.

Once a star’s period P was identified, we binned the phased light curve to 100 points per cycle. To separate “sharp” local minima from smooth spot-induced variability, we then iteratively fit robust penalized splines to the wrapped phase-folded light curve, excluding points more than two standard deviations away from the local continuum (Hippke et al. 2019). The maximum number of equidistant spline knots per cycle is the parameter in this framework that controlled the meaning of “sharp”—we allowed at most 10 such knots per cycle, though for most stars fewer knots were preferred based on cross-validation using an ℓ^2 -norm penalty. An example fit is shown in panel (e) of Figure 2.

We then identified local minima in the resulting residual light curve using the SciPy `find_peaks` utility (Virtanen et al. 2020), which is based on comparing adjacent values in an array. For a peak to be flagged as significant, we required it to have a width of at least $0.02P$, and a height of at least twice the point-to-point RMS. This latter quantity is defined as the 68th percentile of the distribution of the residuals from the median value of $\delta f_i \equiv f_i - f_{i+1}$, where f is the flux and i is an index over time.

To identify local minima near the edges of the phased light curve, which usually would cover phases $\phi \in [0, 1]$, we performed the entire procedure over a phase-folded light curve spanning $\phi \in [-1, 2]$, by duplicating and concatenating the ordinary phase-folded light curve. The free parameters we adopted throughout this analysis procedure, for instance the maximum number of spline knots per cycle, and how large and wide of a local minimum to consider a “true dip”, were chosen during testing based on their ability to correctly re-identify a large fraction ($>90\%$) of known CQVs, while also being able to consistently reject common false positives such as rapidly rotating spot-induced variability and typical eclipsing binaries.

Overall, for a star to proceed to manual examination, we required that it have a peak PDM period below two days, and that it exhibited at least three sharp local minima (as algorithmically reported) in at least one observed TESS sector.

2.2.2. Fourier analysis

We performed an independent search for strongly periodic phenomena using a Fourier-based approach, following Zhan et al. (2019) and Pribulla et al. (2023, their Section 1.3). Starting with the PDC_SAP light curves, we normalized each light curve, and then re-binned it into equal width bins **LB: how long?** to account for the uneven spacing in the TESS data, as well as the data gap during each sector caused by satellite downlink. We then padded the data to ensure that the light curve had a length that was a power of two, as described by Zhan et al.. We then took the Fourier transform of the corrected, padded light curve using `numpy.fft.fft` and searched for peaks with a significance of over 12σ within each set of 500 bins.

If a peak of such significance was found, we generated a “summary sheet” with information about the star, its full

and folded light curves, Fourier transform, potential contaminating stars, and information about these contaminating stars. In the sectors for which we performed this analysis, we found that “summary” sheets were generated for $\approx 10\%$ of the 20 000 120-second targets in a given sector. We then manually reviewed each summary sheet, and visually labelled each star based on its morphology (including e.g., eclipsing binary, CQV, RS CVn, or cataclysmic variable). CQVs that were observed in multiple sectors had their light curves stitched together and analyzed for a more accurate period determination.

2.2.3. Manual vetting

We assessed whether the objects found using the dip-counting (Section 2.2.1) and Fourier (Section 2.2.2) techniques were consistent with expectations for CQVs by assembling the data shown in Figure 2. We labeled a star as a “good” CQV if at least one TESS sector showed what we viewed as the unambiguous signatures of the class (short period; at least three dips or else otherwise oddly-shaped dips; relative stability over a timescale of 30 days). We independently noted stars that we thought could be CQVs, but that were more ambiguous.

Broadly speaking, the most common false positives for both the Fourier and dip-counting techniques were eclipsing binaries, spot-induced variability from rapid rotators, and variability from neighboring, off-target stars. Typical false positive rates from our dip-counting pipeline were 5:1, with 368 unique stars flagged, and about 20% being labeled either “good” or “possible” CQVs. The Fourier analysis was not amenable to calculating a similar false-positive probability, because it was implemented as a general variability search; its results are also being used for other types of variability analyses beyond CQVs.

2.3. Stellar properties

Ages—We estimated the stellar ages by making probabilistic spatial and kinematic associations between the CQVs and known clusters in the solar neighborhood. For most stars in our sample, we did this using BANYAN Σ (Gagné et al. 2018).¹ This algorithm calculates the probability that a given star belongs to one of 27 young clusters (or “associations”) within 150 pc of the Sun, by modeling the clusters as multivariate Gaussians in 3-D position and 3-D velocity space. We used the Gaia DR2 sky positions, proper motions, and distances to calculate the membership probabilities. BANYAN Σ in turn analytically marginalizes over the radial velocity dimension. The probabilities returned by this procedure are qualitatively useful, but should be assessed with caution due to the non-Gaussian nature of most groups within the solar neighborhood (see e.g. Kerr et al. 2021, Figure 10).

For a few cases where BANYAN Σ yielded ambiguous results, we consulted the meta-catalog of young, age-dated,

¹ https://github.com/jgagneastro/bayan_sigma, git commit 394b486



Figure 2. Validation plots used to label CQVs. The complete figure set, with one image per sector for each of 70 CQVs and CQV candidates is available online For internal collaboration review: <https://www.dropbox.com/scl/fo/zlj3txot4cvymfb22wewu/h?dl=0&rlkey=3ec5f9o5xewrixzfkhkdenopa>. Panels are as follows. *a*): Phase-folded light curve; gray points are raw 2-minute data and black points are binned to 200 points per cycle. *b*): Phase-dispersion minimization (PDM) periodogram. Dotted lines show up to the 10th harmonic and subharmonic. *c*): DSS finder chart, with 1- and 2-TESS pixel radius circles displayed for scale. *d*): Cleaned light curve, binned to 20-minute cadence, in Barycentric TESS Julian Date (BTJD). *e*): Phase-folded light curve, binned to 100 points per cycle. The gray line denotes the automated spline-fit to the wrapped phase-folded light curve, and small gray triangles denote automatically identified local minima. *f*): Phase-folded light curve at twice the peak period. *g*): Phase-folded light curve at half the peak period. *h*): Phase-folded time-series within the “background” aperture defined in the SPOC light curves. *i*): Phase-folded flux-weighted centroid in the column direction. *j*): Phase-folded flux-weighted centroid in the row direction. *k*): Gaia DR2 color-absolute magnitude diagram. The gray background denotes stars within 100 pc. *l*): Information from Gaia DR2, TIC8, and the automated dip-counting search pipeline. “Neighbors”, abbreviated “nbhr”, are listed within apparent distances of 2 TESS pixels if $\Delta T < 2.5$. *m*): BANYAN- Σ v1.2 association probabilities, calculated using positions, proper motions, and the parallax.

and age-dateable stars within a kiloparsec from Bouma et al. (2022), and also searched the local volume around each star for co-moving companions.²

Effective temperatures, radii, and masses—We determined the stellar effective temperature and radii by fitting the broadband spectral energy distributions (SEDs); we then estimated the masses by interpolating against the sizes, temperatures,

and ages against the PARSEC v1.2S models (Bressan et al. 2012; Chen et al. 2014).

For the SED fitting, we used `astroARIADNE` (Vines & Jenkins 2022). We adopted the BT-Settl stellar atmosphere models (Allard et al. 2012) assuming the Asplund et al. (2009) solar abundances, and the Barber et al. (2006) water line lists. The broadband magnitudes we considered included $GG_{BP}G_{RP}$ from Gaia DR2, $Vgri$ from APASS, JHK_S from 2MASS, SDSS r_{iz} , and the WISE 1-2 passbands. We omitted UV flux measurements from our SED fit to avoid any possible bias induced by chromospheric UV excess; we

² <https://github.com/adamkraus/Comove>, git commit 278b372

similarly omitted WISE 3-4, but due to reliability concerns. `astroARIADNE` compares the measured broadband flux measurements against pre-computed model grids, and by default fits for six parameters: $\{T_{\text{eff}}, R_*, A_V, \log g, [\text{Fe}/\text{H}], d\}$. The distance prior is drawn from [Bailer-Jones et al. \(2021\)](#). The surface gravity and metallicity are generally unconstrained. And finally, given our particular use-case, we assumed the following priors for the temperature, stellar size, and extinction:

$$T_{\text{eff}}/\text{K} \sim \mathcal{N}(3000, 1000), \quad (5)$$

$$R_*/R_\odot \sim \mathcal{T}_{\text{N}}(0.5, 0.3, 0.1, 1.5), \quad (6)$$

$$A_V/\text{mag} \sim \mathcal{U}(0, 0.2), \quad (7)$$

for \mathcal{N} the Gaussian and \mathcal{U} the uniform distributions, and $\mathcal{T}(\mu, \sigma, a, b)$ a truncated normal distribution with mean μ , standard deviation σ , and lower and upper bounds a and b . We validated our chosen upper bound on A_V using a 2MASS color-color diagram. Finally, using `Dynesty` ([Speagle 2020](#)), we sampled the posterior probability assuming the default Gaussian likelihood, and set a stopping threshold of $d\log \mathcal{Z} < 0.01$, where \mathcal{Z} denotes the evidence.

With the effective temperatures and stellar radii from the SED fit, we then estimated the stellar masses by interpolating against the PARSEC isochrones (v1.2S [Chen et al. 2014](#)). The need for models that incorporate some form of correction for young, active M dwarfs is well-documented (e.g. [Stassun et al. 2012](#); [David & Hillenbrand 2015](#); [Feiden 2016](#); [Somers et al. 2020](#)). Plausible explanations for anomalous M dwarf colors and sizes relative to model predictions include starspot coverage (e.g. [Gully-Santiago et al. 2017](#)), and potentially incomplete line lists (e.g. [Rajpurohit et al. 2013](#)). In the PARSEC models, [Chen et al. \(2014\)](#) performed an empirical correction to the temperature–opacity relation drawn from the BT-Settl model atmospheres, in order to match observed masses and radii of young eclipsing binaries. This is sufficient for our goal of estimating stellar masses. Given our observed $\{\tilde{T}_{\text{eff}}, \tilde{M}_*, \tilde{t}\}$, and approximating their uncertainties as Gaussian $\sigma_{\tilde{T}_{\text{eff}}}$, $\sigma_{\tilde{M}_*}$ and $\sigma_{\tilde{t}}$, we evaluate a distance d between our observations and any model PARSEC grid-point $\{T_{\text{eff}}, M_*, t\}$ as

$$d^2 = \left(\frac{\tilde{T}_{\text{eff}} - T_{\text{eff}}}{\sigma_{\tilde{T}_{\text{eff}}}} \right)^2 + \left(\frac{\tilde{M}_* - M_*}{\sigma_{\tilde{M}_*}} \right)^2 + \left(\frac{\tilde{t} - t}{\sigma_{\tilde{t}}} \right)^2, \quad (8)$$

in order to assign equal importance to each dimension. The preferred model mass is then one that minimizes this distance, and is quoted in Table 1. **Igb todo: real interpolation, rather than nearest neighbor**

3. RESULTS

3.1. CQV catalog

Table 1 lists the 70 objects identified by our search. The “high-quality sample” includes 53 of these objects, which demonstrated what we viewed as unambiguous characteristics of the CQV phenomenon in at least one TESS sector. The classification of the remaining 14 CQV candidates

was ambiguous. Additional data from TESS or other instruments could help resolve their classification. The boolean `quality` column in the table divides the two classes. In the following, we will restrict our discussion to the high-quality sample.

The mosaic in Figure 3 shows phased light curves for the 53 CQVs. The objects are sorted first in order of the number of TESS 120-second cadence sectors in which they clearly demonstrated the CQV phenomenon, and secondarily by descending brightness. The top five objects by this metric are TIC 300651846 ($T=13.5$, 12 sectors); TIC 402980664 ($T=11.1$, 7 sectors); TIC 89463560 ($T=13.5$, 5 sectors); TIC 363963079 ($T=12.9$, 5 sectors); and TIC 294328887 ($T=14.2$, 4 sectors). The brightest five CQVs span $9.3 < T < 11.1$; the faintest five span $14.5 < T < 15.0$. The fastest five have periods spanning $3.6 \text{ hr} < P < 6.2 \text{ hr}$, and the slowest five span $27 \text{ hr} < P < 38 \text{ hr}$. Regarding likely astrometric or visual binaries, 9/53 high-quality CQVs have a Gaia DR2 RUWE > 2; 1/14 of the ambiguous sample share this characteristic.

In terms of the light curve shapes, Figure 3 shows a broad range of variability, with anywhere from two to eight local minima per cycle. Some stars show relatively ordinary modulation during one portion of the phased light curve, and highly structured modulation in the remainder of the cycle (e.g. TIC 206544316, TIC 224283342, TIC 402980664). Others show structured modulation over the entire span of a cycle (e.g. TIC 2234692, TIC 401789285, TIC 425933644, TIC 142173958). Others show some mix between these two modes.

A small number of objects at first glance seem reminiscent of eclipsing binaries, such as TIC 193831684 or TIC 5714469. In these few cases, we believe that that are unlikely to be eclipsing binaries due to additional coherent variations in the light curves that are distinct from any binary phenomenology of which we are aware.

3.2. Ages

Of our 70 confirmed and candidate CQVs, 64 were associated with a nearby moving group or open cluster using BANYAN Σ . The relevant groups are listed in Table 1; their ages span $\approx 5\text{--}200$ Myr. The most prodigious groups were Sco-Cen, Tuc-Hor, and Columba. Six CQVs were also identified in the Argus association ([Zuckerman 2019](#)), which serves as an indirect line of evidence supporting the reality, and youth, of that group. The yield in Sco-Cen is not surprising, since Sco-Cen contains the majority of pre-main-sequence stars in the solar neighborhood. However, given the $\lesssim 10\%$ completeness of TESS beyond 100 pc, there are probably many more CQVs that remain to be discovered in Sco-Cen.

Of the three stars for which BANYAN Σ did not find any association, one (TIC 302160226) is a member of α Per ($t \approx 86 \pm 16$ Myr; [Meingast et al. 2021](#); [Boyle & Bouma 2023](#)). For the other two (TIC 58084670 and TIC 141146667), we were not able to confidently associate either star with any young groups. However both do seem to show the CQV sig-

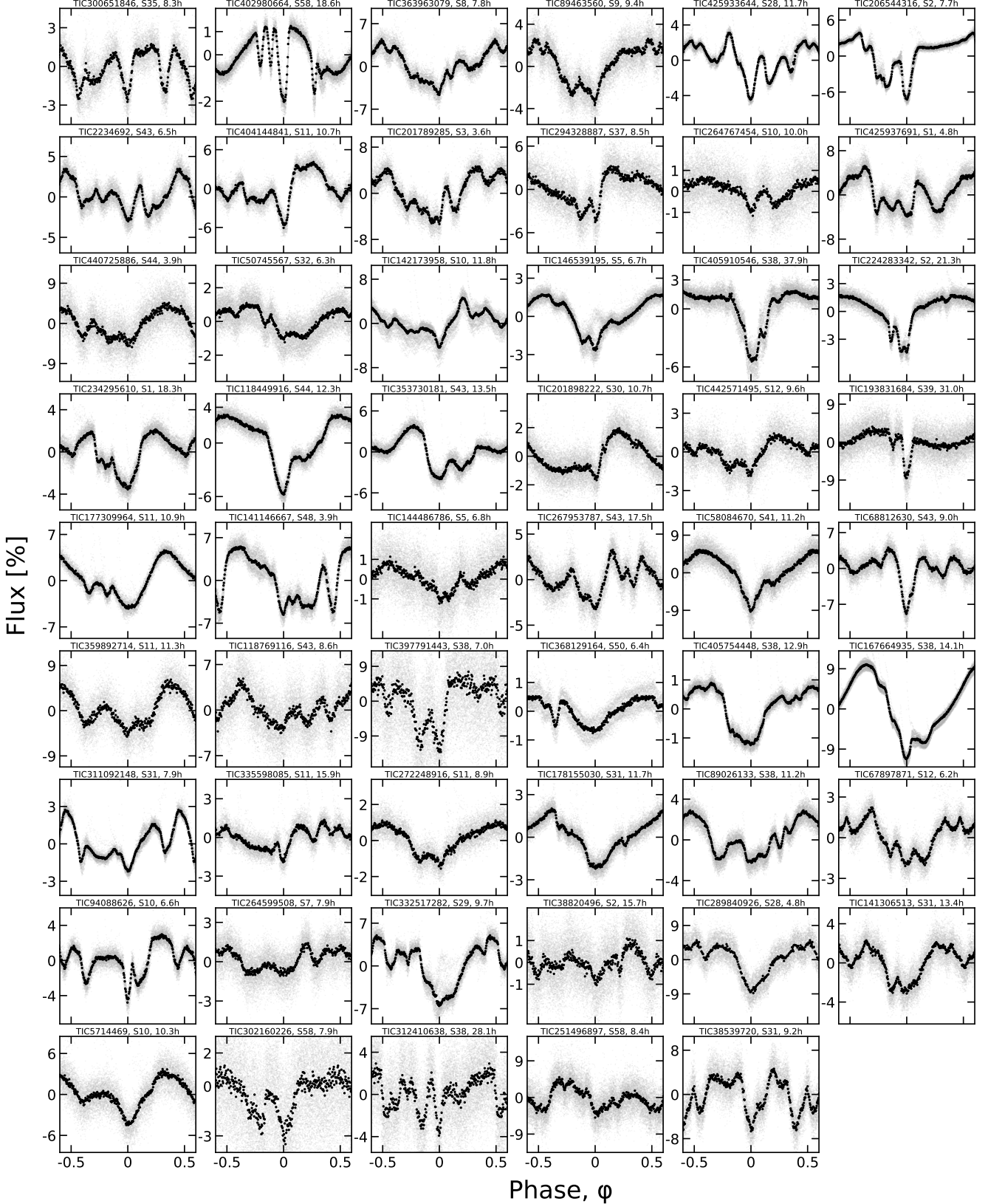


Figure 3. CQVs found in the TESS 2-minute data. Phased TESS light curves over one month are shown for 53 CQVs in the high quality sample. Gray are raw 2-minute data; black bins to 300 points per cycle. Each panel is labeled by the TIC identifier, the TESS sector number, and the period in hours. Objects are ordered such that sources with the most TESS data available are on top (see Section 3.1).

nal over multiple TESS sectors, and both are photometrically elevated relative to the main sequence. For instance, both were noted by Kerr et al. (2021) as being in the “diffuse” population of <50 Myr stars near the Sun.

Our search confirms that the CQV phenomenon persists for at least ≈ 150 Myr. Table 1 includes three ≈ 150 Myr CQVs in AB Dor (Bell et al. 2015), a ≈ 112 Myr old Pleiades CQV (Dahm 2015), and a similarly-aged Psc-Eri member (Ratzenböck et al. 2020). To our knowledge, TIC 332517282 in AB Dor was the previous record-holder for oldest-known CQV (Zhan et al. 2019; Günther et al. 2022); at least one unambiguous CQV (EPIC 211070495) and a few other candidates were also previously known in the Pleiades (Rebull et al. 2016).

The upper age limit for CQVs may even pass 200 Myr, based on the candidate membership of TIC 294328887 in the Carina Near moving group (Zuckerman et al. 2006). This group’s 200 ± 50 Myr age is based on the lithium sequence of its G-dwarfs (Zuckerman et al. 2006), which shows a co-eval population of stars older than the Pleiades and younger than the 400 Myr Ursa Major moving group. The formal BANYAN- Σ membership probability is however somewhat low, perhaps due to the missing radial velocity. This could be resolved by acquiring even a medium-resolution spectrum. An independent assessment of the group’s kinematics using Gaia data, and its rotation sequence using TESS, could lend further credence in such an analysis.

3.3. Infrared excesses

Most CQVs in our catalog did not show infrared excesses in the W1-W4 bands, which is typical for this class of object (Stauffer et al. 2017). Visually inspecting the SEDs of our 70 star sample, we labeled two objects as having “good” infrared excesses (both W3 and W4 at $>3\sigma$ above the photospheric prediction), and three as “possible” infrared excess (only W3 at $>3\sigma$).

The two “good” IR excesses belonged to TIC 193136669 (TWA 34) and TIC 57830249 (TWA 33). Both are in the TW Hydreae association (≈ 10 Myr), and have relatively long periods of 38 hr and 44 hr respectively. In our initial labeling, we labeled both as “ambiguous” CQVs because the dips in their light curves did not show the rigid periodicity typical of CQVs; their periods were also relatively long. However, inspection of further sectors clarified that both sources are dippers (see online plots in Figure 2). Independently, TIC 193136669 has a cold molecular disk based on observed 1.3 mm continuum emission and resolved Keplerian $^{12}\text{CO}(2-1)$ emission (Rodriguez et al. 2015). It was also labeled a dipper by Capistrant et al. (2022); we agree with their designation, and label it an “impostor” CQV in Table 1. TIC 57830249 (TWA 33) also has previously detected 1.3 mm continuum emission (Rodriguez et al. 2015), suggestive of cold dust grains being present. It is also a dipper. Section 5.7 highlights plausible evolutionary connections between CQVs and dippers in light of these “misclassifications”.

Our three “possible” infrared excesses were TIC 405910546, 289840926, and 244161191. After a lit-

erature search, we concluded that none have clear evidence for the presence of a disk. TIC 405910546, in LCC, shows a unique TESS light curve, reminiscent of a $P=38$ hr singly-eclipsing binary, except with additional substructure during each eclipse that resembles the CQV phenomenon more than any other variability of which we are aware. TIC 289840926 (β Pic moving group, $P=4.8$ hr), shows what we believe is a clear CQV signal, but has no definitive evidence for a large, dusty disk. TIC 244161191 (TOI-278), in Columba, also has no definitive evidence for a large disk. It is however “multi-periodic”—in addition to the 7.17 hr CQV signal, this source shows a superposed 8.39 hr sinusoidal signal, probably from an unresolved neighboring star or binary companion.

4. CQV EVOLUTION

4.1. Evolution over two year baseline

Figure 4 shows “before” and “after” views of 27 CQVs for which TESS 120-second cadence observations were available at least two years apart. Such a baseline was available for 32 of the confirmed 53 CQVs in our catalog; for plotting purposes we show the brightest 27. We have phased each sector to its own local minimum because for most of the sources we do not know the period at the precision necessary to be able to accurately propagate an ephemeris over two years. The achievable period precision, σ_P , can be estimated as

$$\sigma_P = \frac{\sigma_\phi P}{N_{\text{baseline}}}, \quad (9)$$

for N_{baseline} the number of cycles in the observed baseline and σ_ϕ the phase precision with which any one feature (e.g. a dip, or the overall shape of the sinusoidal envelope) can be tracked. Assuming $\sigma_\phi \approx 0.02$ and a 20-day baseline over a single TESS sector yields $\sigma_P \approx 0.25^{+0.38}_{-0.14}$ minutes for the population shown in Figure 4; propagated forward 1,000 cycles yields a typical ephemeris uncertainty range of 2-11 hours. Measuring the periods for each sector independently, there did not seem to be any significant ($>3\sigma$) period changes. This implies an absolute period stability of $\lesssim 0.1\%$ over the two-year baseline.

Of the 27 CQVs in Figure 4, a few show clear signs of the CQV phenomenon in one sector, and marginal or non-existent signs in the other. While there is subjectivity in this assessment, to our eyes cases for which at least one sector would be flagged as “ambiguous” include TIC 368129164 (Sector 23 might be labeled an EB), TIC 177309964 (Sector 38 would be simply a rotating star), TIC 404144841 (Sector 38 looks like a rotating star), TIC 201898222 (Sector 3 looks like a rotating star), TIC 144486786 (Sector 32 might be an RS CVn), and TIC 38820496 (Sector 28 might be an RS CVn). TIC 193831684, assessed on a single-sector basis, would probably be labeled an eclipsing binary—in fact, Justesen & Albrecht (2021) implicitly have already given this source such a label. However, based on the the shape evolution between Sectors 13 and 39, it is a CQV. Based on the fraction of sources overall that “turned off”, the observed shape evolution implies that CQVs have a duty cycle of $\approx 75\%$. This type of correction is worth including

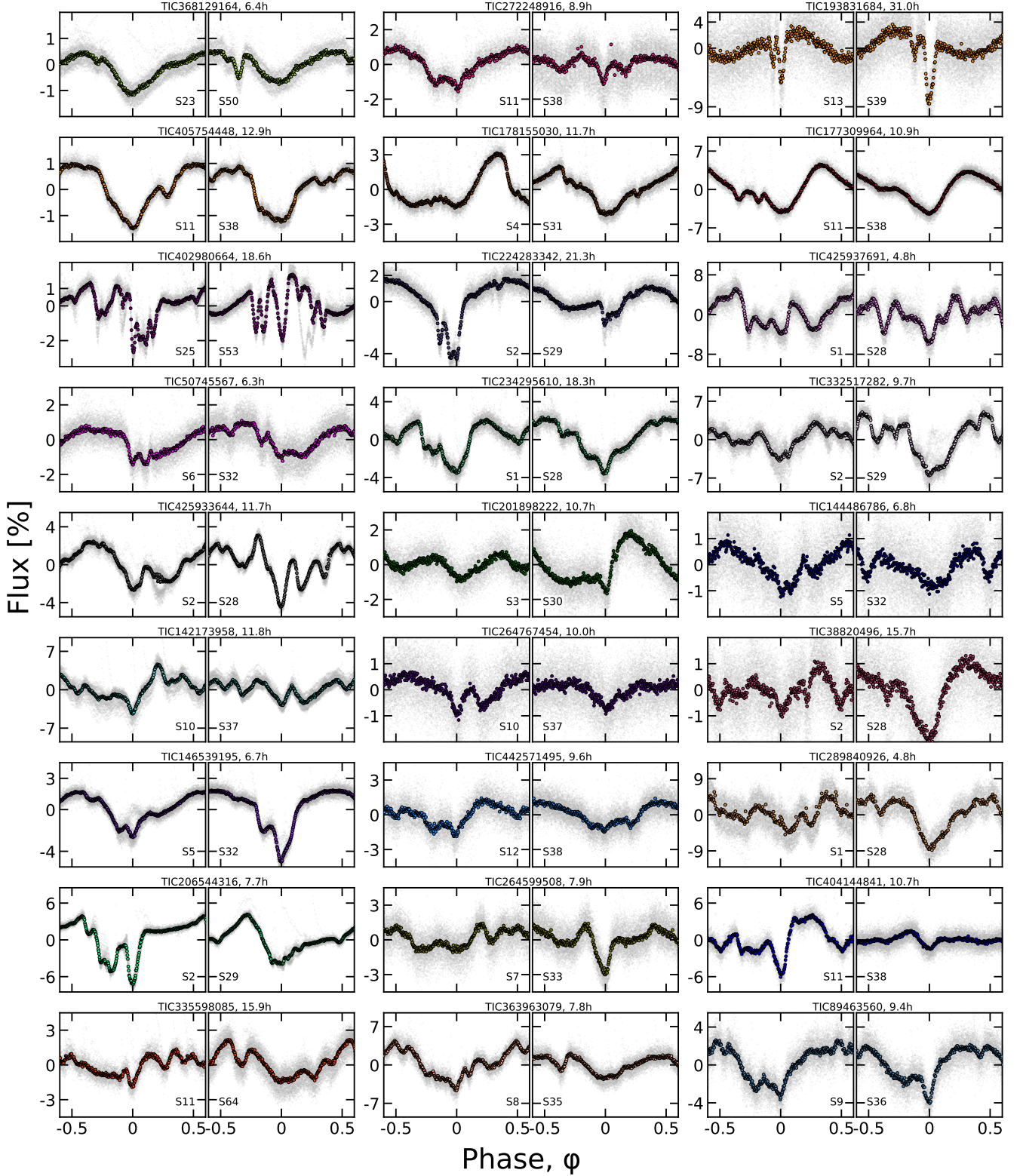


Figure 4. CQVs keep their periods but change their shapes. Out of the 53 CQVs in Figure 3, 32 had 120-second cadence TESS data available for a baseline of at least two years; the 27 brightest are shown here due to space constraints. Each panel shows one sector of TESS data, and is phased to its deepest minimum in flux. Each panel's title shows the TIC identifier and approximate period in hours. Text insets show the TESS sector numbers, which generally span two years, or at least 1,000 cycles. The vertical scale is fixed across sectors to clarify shape changes. Gray circles are raw 2-minute data; colored circles bin to 300 points per cycle.

in population-level estimates of how intrinsically common CQVs are in the low-mass stellar population (e.g. Günther et al. 2022).

4.2. Evolution over adjacent sectors, & LP 12-502

Out of the 53 CQVs, a small fraction were in regions of sky with many sectors of adjacent TESS data. Out of these objects, LP 12-502 (TIC 402980664; $d=21\text{ pc}$, $J=9.4$, $T=11.1$) stood out due to the quality and content of its data. We describe another interesting source, TIC 300651846, in Appendix A. In this section, we first present the LP 12-502 observations (Section 4.2.1), and then highlight their implications (Section 4.2.2).

4.2.1. LP 12-502 observations

Figure 5 shows all available data for LP 12-502 from TESS Sectors 18, 19, 25, 26, 53, 58, and 59, split into successive orbits. The star was observed at 120-second cadence whenever it was observable by TESS. We binned the light curve to 15-minute intervals for visual clarity, and required at least one (120-second cadence) flux measurement per bin. Points more than 2.5σ above the median are drawn in gray, also for visual clarity. Missing data are not drawn. Figure 6 then shows the same data, but stacked into successive TESS orbits spanning half a lunar month each. Finally, Figure 7 shows “river plots” of the same data, split into similar intervals: the Sector 18-19 data, 25-26 data, 53 data, and 58-59 data. The river plots are subject to one additional processing step: we fitted and subtracted a maximum-likelihood two-harmonic sinusoid independently from the Sector 18-19 data, 25-26 data, and 53, 58, and 59 data in order to accentuate changes in the dip timing and structure.

The average period, determined by measuring the PDM peak period over each sector independently, was $\langle P \rangle = 18.5560\text{ hr}$. The range between the maximum and minimum sector-specific periods was measured to be about one minute. However, in detail, a period shift of ± 1 minute would yield major phase drifts over the baseline; that time interval corresponds to $\approx 1/1000^{\text{th}}$ of a period, and we have observed 1500 cycles. By fine-tuning over a grid in period, we found $P = 18.5611 \pm 0.0001\text{ hr}$, which seems to track certain features in the LP 12-502 light curve well over the entire dataset.

What exactly is observed? For the first 64 cycles, the star shows a pattern reminiscent of an eclipsing binary, with four obvious local minima. We dub these dips $\{1, 2, 3, 4\}$ at phases $\{-0.28, -0.08, 0, 0.25\}$, respectively. Over cycles 0-64, the depth of dips 1 and 3 remain roughly fixed. However dip 4 decreases in depth by about 2%, while dip 2 increases in depth, by about the same amount (see Figure 6). During cycles 48-64, a fifth dip may also be emerging, in the main “large” dip group.

There is then a 6-month (184 cycle) gap to Cycles 248-315, which show two highly structured dip complexes, plus a small leading dip. The single leading dip is present at the same phase as in cycles 0-64, and is therefore likely to be the same structure. Along a similar line of logic, it seems plausible that the first “dip complex” during cycles 248-264

represents an evolution of the initial complex seen during cycles 0-64, though with reduced depth. During cycles 266-310, an additional local minimum develops between the two complexes; this feature is best visualized on the river plots (Figure 7), and we describe its (shorter) period below.

The second dip complex during cycles 248-315 shows the most substructure. During e.g. cycles 283-298, this single complex shows six local minima. The deepest dip is sharp: it shows a flux excursion of 3.5% over about 22 minutes ($0.02 P$), which is the steepest slope exhibited anywhere in the LP 12-502 dataset. After the sharp dip, there is a roughly exponential fall-off spanning about a quarter of a period, punctuated by coherent local minima and maxima which in detail (Figure 7) have slightly longer periods than the sharp dip. The sharp leading dip only decreases in depth following a sudden state-switch at BTJD 2030.7 (cycles 299-315), which happens during a flare (Figure 5). The trailing dips remain thereafter.

Sectors 53-58 (cycles 1233-1481) are comparatively tame; they showed only four to six dips per cycle. Some dips remain stable in depth and duration over this five month interval. Other dips grow, like the one at $\phi = +0.06$ between cycles 1499 and 1481. Other dips, such as the one at $\phi = +0.12$ in cycles 1233-1264, disappear entirely. The most dramatic state switch occurs during cycles 1233-1247, when a large dip “switches” from a depth of 3% and duration of 3 hours to a depth of 0.3%, and a duration of 1 hour.

4.2.2. Lessons from LP 12-502

STATE-SWITCHES REVEAL DIP INDEPENDENCE—The state-switches seen in cycles 1233-1247 and 299-315 confirm that dips can disappear in less than one cycle, a point which has been previously appreciated (Stauffer et al. 2017). What is new in these particular changes is that the morphology changes show that the dips can be *independent* and *additive*. For example, throughout cycles 1233-1264, there are three local minima between phases of 0 and 0.3. They all have identical ingress times. The shape change during the transition implies that the leading dip that “turned off” (reduced its depth and duration), while the trailing two dips remained fixed. This is visible in Figure 6. In other words, the structures producing these dips are independent to the degree that one can undergo a severe change while the others remain identical. The state switches during cycles 248-264 and 299-315 share the same characteristic: it is always the *leading* dip of a complex that “switches off”, leaving the (fixed-depth) trailing dips in its wake.

SLOW GROWTH; RAPID DEATH—Although there are a few instances in which we observe dips switch off over less than one cycle, dip growth seems to happen more slowly. For instance, the dip that grows between phase 0 and 0.1 between cycles 260-290 begins to become visible around BTJD 1993.2, and grows in depth by about 2% over about six cycles, to become visible by eye by BTJD 1997.7. The evolution of this particular dip is most clear in the river plots. The evolution of the latter dip group in cycles 1410-1481 is another example of this slow mode of dip growth.

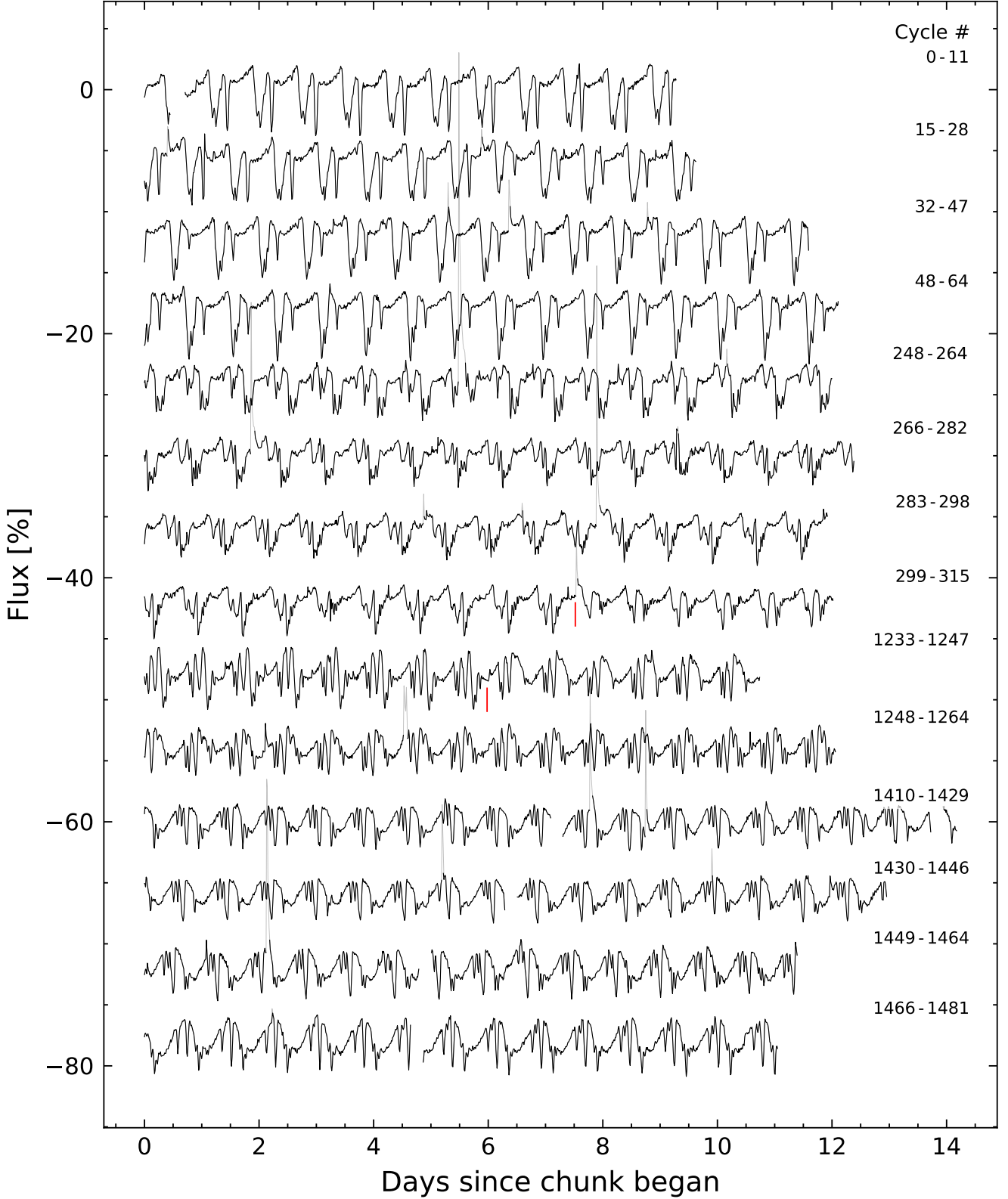


Figure 5. LP 12-502 (TIC 402980664) light curve, where each time chunk represents one TESS orbit. Data were acquired in Sectors 18-19, 25-26, 53, and 57-58. Flares are drawn in gray. The red vertical lines highlight apparently instantaneous state changes in the shape of the dip pattern. The light curve is binned to 15-minute intervals so that there are 96 points per day, and each point is connected by a line. Data gaps longer than 15-minutes are not interpolated; if data are missing, nothing is plotted.

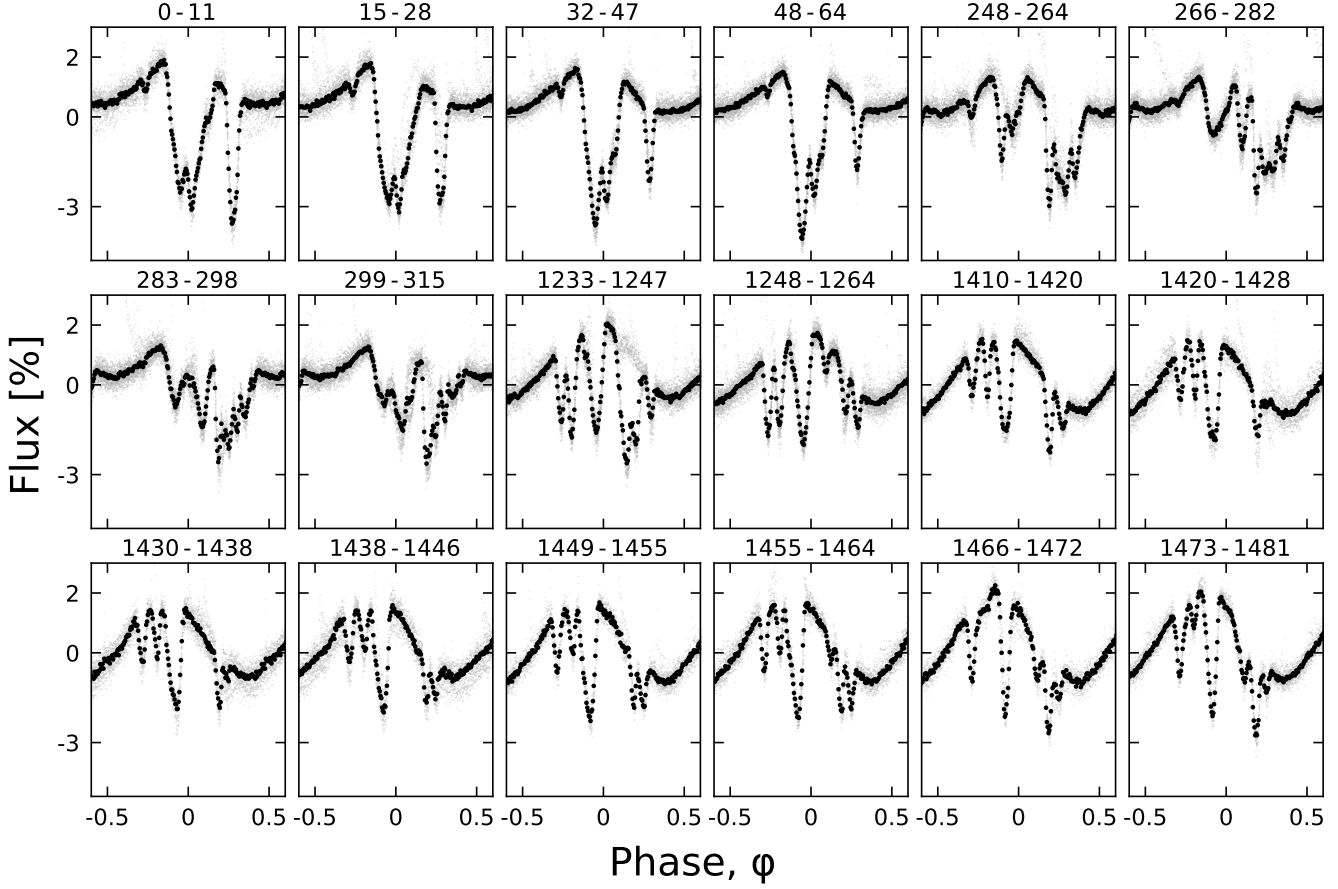


Figure 6. Evolution of LP 12-502 ($P=18.6$ h) at fixed period and epoch over three years. Each panel shows one (stacked) TESS orbit; small text denotes relative cycle number. There are 200 binned black points per cycle. The TESS pointing law dictates the large time gaps between Cycles 64-248, 315-1233, and 1264-1410; larger gaps tend to yield larger shape changes. The dips usually evolve over tens to hundreds of cycles. However cycles 1233-1264 show a dip that “switched” from a depth and duration of 3% and 3 hr to 0.3% and 1 hr over less than one cycle (cf. Figure 5).

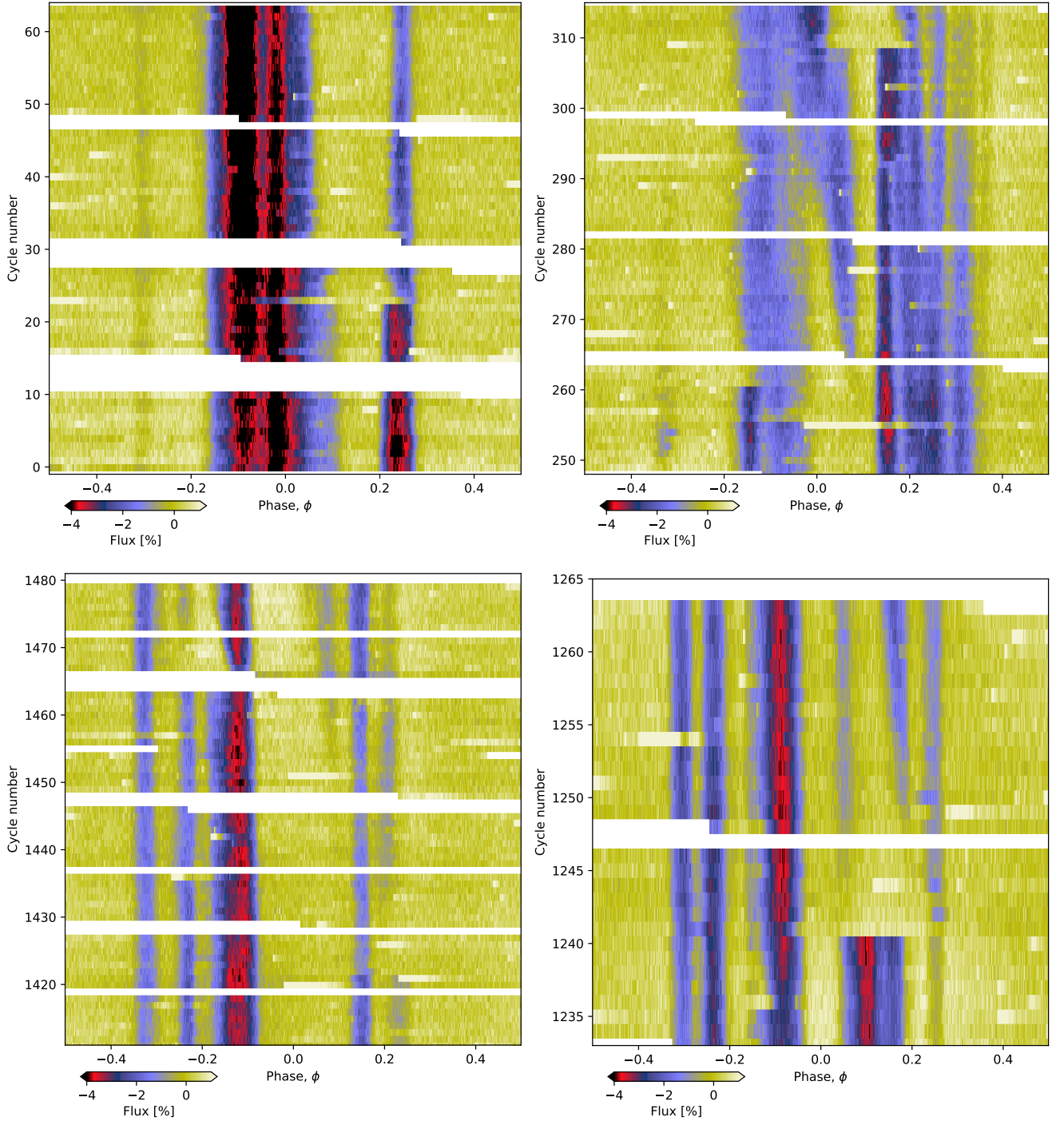


Figure 7. River plots of the LP 12-502 light curve, showing (clockwise from top-left) Sectors 18-19, 25-26, 53, and 58-59. A two-harmonic sinusoid has been subtracted to highlight the sharp dips. In Sectors 25-26 (cycles 248-315), periods are visible at the fundamental period of 18.5611 hr, as well as at faster and slower relative periods (e.g. $\phi \approx 0.3$ and $\phi \approx 0.1$). Similar instances of multiple simultaneous periods are also visible in Sector 53 and 58-59. White chunks denote missing data.

DIP DURATIONS—The shortest dip duration for any of the individual LP 12-502 dips seems to be $\approx 0.06 P \approx 1.08$ hr. In comparison, using the stellar radius and mass derived in Section 2.3, the characteristic timescale $T_{\text{dur}} \equiv R_{\star}P/(\pi a)$ for the transit of a point-source at corotation is 1.02 ± 0.10 hr. This means that while some of the LP 12-502 dips are sufficiently long to require structures that are extended in orbital azimuth, the durations of other dips are consistent with effective radii for the occulting material $R_{\text{eff}} \ll R_{\star}$. This implies $a/R_{\star} \approx 5.8$ for this material; the analogous timescale at the stellar surface is about six times slower.

DIP PERIODS—Most of the LP 12-502 dips recur with a period of $P = 18.5611 \pm 0.0001$ hr. However the river plots (Figure 7) reveal multiple distinct periodicities in the light curve for specific dips. For instance, in sectors 25–26, the local minimum that develops around cycle 262 has a period faster than the mean period by $\approx 0.1\%$, while some of the trailing local minima in the main dip complex have periods slower than the mean period, by $\approx 0.04\%$. In addition to the fundamental period, we were able to identify at least four distinct periods shown by specific dips over the full Sectors 18–59 dataset, including periods at 18.5683, 18.5672, 18.5473, and 18.5145 hr, with a typical measurement uncertainty of ≈ 0.0002 hr. If each period corresponds to an individual dust or gas clump, then this implies that multiple distinct clumps can orbit the star simultaneously, at marginally different separations.

5. DISCUSSION

5.1. Typical and extreme CQVs

Figure 8 shows derived stellar properties for our CQV catalog, and compares the CQVs against both the target star sample (top panels), and against stars in the Pleiades (Rebull et al. 2016). Typical CQV masses span $0.1\text{--}0.4 M_{\odot}$, and typical ages span 2–150 Myr. This mass and age range includes both fully convective stars ($M_{\star} \lesssim 0.25 M_{\odot}$), and stars with a combination of radiative cores and convective envelopes ($M_{\star} \gtrsim 0.25 M_{\odot}$; Baraffe & Chabrier 2018). We found no obvious morphology differences between the two classes, which is somewhat surprising given that the star’s interior structure may influence the field topology (Reiners & Basri 2009). In terms of their rotation rates relative to the Pleiades, the CQVs are among the more rapidly rotating half of M dwarfs, in our sample, despite our search extending to $T=16$, is a consequence of the 120-second selection function, not detection sensitivity.

The closest CQV in our catalog is DG CVn (TIC 368129164; $d=18$ pc), a member of AB Dor. To our knowledge, this manuscript is the first time that it has been noted as a CQV. The three brightest CQVs are DG CVn ($T=9.3$), TIC 405754448 ($T=9.6$), and TIC 167664935 ($T=10.3$). The shortest period belongs to TIC 201789285, at 3.64 hr. The longest period belongs to TIC 405910546, at 37.9 hr. If the latter source turns out to be an eclipsing binary, the next-longest would be TIC 193831684 (31.0 hr).

The lowest mass ($\approx 0.12 M_{\odot}$) belongs to TIC 267953787. The catalog contains a few other stars with similar mass.

Given the small number of sub-stellar mass objects in our target sample, future studies of brown dwarf photometric variability might also yield CQVs, though there could be degeneracies in interpretation with planetary surface features such as clouds and latitudinal bands (e.g. Apai et al. 2021; Vos et al. 2022).

5.2. Binaries, massive CQVs, and a new class of false positive

The high-RUWE objects in Figure 8 tend to be among the more massive half of the CQV sample. This suggests that either that the RUWE indicator is not sensitive to binarity among lower mass stars, or that these “high-mass CQVs” may be unresolved blends in which the lower mass companion is produces the CQV signal.

5.2.1. Do K dwarf CQVs exist?

The two most massive CQVs in our sample present a relevant case study. To date, the only stars reported to show the CQV phenomenon are M dwarfs, with typical stellar masses $\lesssim 0.3 M_{\odot}$ (Stauffer et al. 2017; Günther et al. 2022). TIC 405754448 and TIC 405910546 however appear to have masses of $\approx 0.82 M_{\odot}$ and $\approx 0.60 M_{\odot}$ respectively. The next-highest masses in our sample are $\approx 0.40 M_{\odot}$. The masses for the former two objects are consistent with their locations in the color–absolute magnitude diagram, and with their membership in LCC. However the light curve morphology of TIC 405910546 is unique among the CQV sample, and suggestive of an eclipsing binary; it should be studied further to clarify its classification. For TIC 405754448, we expect that this source is an unresolved binary, because $\text{RUWE}_{\text{DR2}}=4.7$, and because the raw light curves in Sectors 11, 37, and 38 show an additional ≈ 6.5 day, $\approx 0.3\%$ amplitude sinusoidal signal suggestive of an unresolved photometric companion. If TIC 405754448 is a K+M binary, then the flux ratio between the primary and secondary would be expected to be $\approx 10:1$. It would be challenging for the M dwarf to produce the observed 12.9 hr signal with such a flux deficit, but not impossible. While both of these objects suggest that the CQV phenomenon may extend up in mass to pre-main-sequence K dwarfs, more data are needed to fully substantiate this claim.

5.2.2. Systems near the 3:2 commensurability

TIC 435903839—We originally classified TIC 435903839, with $\text{RUWE}_{\text{DR2}}=11.6$, as an “ambiguous” CQV with a 10.82 hr period, because this period minimized the dispersion in the phase-folded light curve. However careful inspection of the periodogram reveals that this source is a photometric blend of two ordinary rotating stars with $P_0=3.60$ hr, and $P_1=5.41$ hr. This is a novel false positive scenario for CQVs: two rapidly-rotating stars with near-integer ratios of rotation periods. The beat between the two rotation signals produces the apparent CQV signal. Such false positives can be excluded through careful accounting of all peaks in a periodogram. For instance, TIC 435903839 shows a peak at 16.27 hr, which is not an integer multiple of the dispersion-

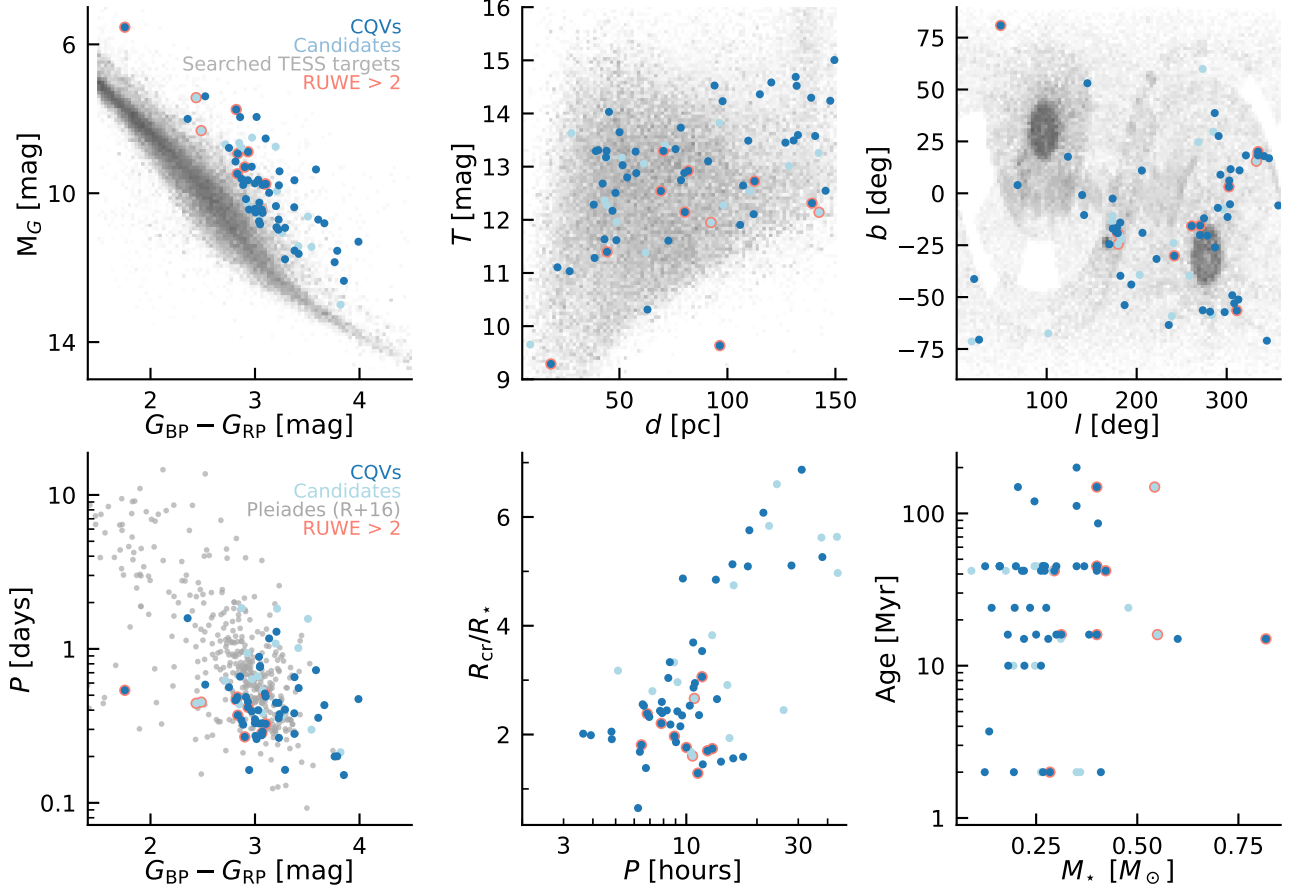


Figure 8. Properties of CQVs identified by our search. CQVs are mostly pre-main-sequence M dwarfs, younger than ≈ 150 Myr, with rotation periods faster than ≈ 1 day. The 53 bona fide CQVs in Table 1 are the dark blue circles; 14 ambiguous CQV candidates are light blue circles. Cases with elevated Gaia DR2 RUWE values are highlighted. The top panels show the 65,760 target stars with 120-second cadence TESS data as the shaded gray background; darker regions correspond to a larger relative number of searched stars. The lower-left panel compares the rotation–color distribution of CQVs against the rotation periods of K and M dwarfs in the Pleiades from Rebull et al. (2016). The lower-middle panel plots the derived corotation radii $R_{\text{cr}} = (GM/\Omega^2)^{1/3}$ in units of stellar radii against the measured CQV periods, in units of hours. Ages in the final panel are known from cluster membership.

minimizing 10.82 hr period. This particular case is an “impostor” CQV.

TIC 425937691—TIC 425937691 is an odd converse case: it shows two seemingly independent CQV signals on what appears to be the same star. The two signals have periods of ≈ 4.82 hr and ≈ 3.22 hr, and so also fall near the 3:2 commensurability. The former is the larger amplitude signal visible in Figures 3 and 4, corresponding to signal with peak-to-peak amplitude of $\approx 8\%$. The latter signal is only visible after subtracting the primary period, and it has a sinusoidal envelope with a peak-to-peak amplitude of 2.5%, and with three sharp dips superposed over each cycle. For TIC 425937691, $\text{RUWE}_{\text{DR2}} = 2.9$.

Given the two photometric signals and the elevated RUWE, this source is probably an unresolved binary consisting of two CQVs. Recent work has shown that the orbits of binaries closer than $\lesssim 700$ AU tend to be aligned with their

planetary systems (Christian et al. 2022). If we assume that observing CQV variability similarly requires near edge-on viewing geometries, then we might expect a sufficiently close binary with one CQV to also have another, since the spin axes in sufficiently close binaries would tend to be aligned. In this scenario, the two periods being within $\approx 0.2\%$ of the 3:2 period commensurability would simply be a coincidence.

5.3. CQVs are quasiperiodic

A periodic signal repeats exactly; the CQVs do not (Figure 4). While their periods appear to remain constant to within measurement precision over thousands of cycles, the light curve shapes evolve over 10 to 1,000 cycles. They are therefore *quasiperiodic*. This observation is consistent studies by Günther et al. (2022) and Popinchalk et al. (2023). However it marks a qualitative departure from the “persistent” vs. “transient” flux dip distinction described by Stauff-

fer et al. (2017); since all CQV dips seem to be transient over timescales of more than 1,000 cycles (Figure 4).

With that said, one might expect a truly quasiperiodic process to be able to explore all phase angles with equal weight. LP 12-502, and perhaps other CQVs, seem to have preferred phases. For LP 12-502, all of the dips happen over phases corresponding to only two thirds of the period (Figure 6). The remaining third seems to be “out of limits” for any dipping material. This could be evidence that some aspect the stellar magnetic field is strongly asymmetric, and can generate and hold extrinsic material at corotation, but only over two thirds of the equatorial circle. Alternatively, the source of the material (e.g. a planetesimal swarm) might be distributed over an arc of the same angular extent (240°). We favor the former explanation, for reasons discussed below.

5.4. Dip asymmetries and dust geometries

The asymmetry of a dip can help diagnose the optical depth of the occulting material as a function of orbital phase angle. Sharp leading edges with trailing exponential egresses for instance have been previously seen for transiting exocomets and disintegrating rocky bodies (e.g. Rappaport et al. 2012; Brogi et al. 2012; Vanderburg et al. 2015; Zieba et al. 2019).

Examining Figure 3, it is not obvious whether CQVs as a whole show any preference for sharper ingresses, or sharper egresses. In some cases (e.g. TIC 425933644), the continuum itself is not well-defined, and so the meaning of “ingress” and “egress” are not clear. In others, such as Sector 36 of TIC 89463560, there is a single clear sharp ingress with an exponential egress, which could be fitted using e.g. a model analogous to those used for exocomets (e.g. Zieba et al. 2019). The main quantities of interest in such models would be the exponential decay time- and therefore length-scale, as well as the impact parameter and the inferred transit depth (and its implications for the equivalent “radius” of the transiting cloud). We briefly explored such models, until it became clear that careful modeling of sources such as LP 12-502 merits its own in-depth study. Connections could likely also be made to the toroidal geometries that can be produced by outflowing atmospheres of transiting planets (e.g. McCann et al. 2019; MacLeod & Oklopčić 2022).

5.5. Dust, or gas?

We believe that the most likely scenarios to explain CQVs are either the dust clump scenario or the prominence scenario (Figure 1). Both invoke clumpy material that would be centrifugally supported at the corotation radius. The prominence idea has a longer history, based on analogy with quiescent prominences/filaments observed to exist in the solar corona for up to a few weeks (see Vial & Engvold 2015). In an extrasolar context, spectroscopic detections of transient Balmer- and resonance-line absorption seen for stars such as AB Dor and Speedy Mic (e.g. Collier Cameron & Robinson 1989; Jeffries 1993; Dunstone et al. 2006; Leitzinger et al. 2016) led to the interpretation that the data could best be explained by similar structures: cold, minimally ionized hydrogen clouds or filaments that scatter chromospheric emission

from the star to produce the observed spectroscopic line variations (see Collier Cameron & Robinson 1989). The short-term mechanical stability of such gas configurations is theoretically plausible (Ferreira 2000; Waugh & Jardine 2022), and the interpretation of this class of observations seems at least somewhat secure.

A clear link between the dense gas clumps (prominences) that likely exist around rapidly rotating low-mass stars and the CQV phenomenon has yet to be made. A simple visual examination of the TESS light curves for five prominence-hosting systems studied by Jardine & Collier Cameron (2019)—AB Dor, Speedy Mic, LQ Lup, HK Aqr, and V374 Peg—revealed no obvious CQV behavior, though all show differential evolution, and Speedy Mic shows two closely-spaced periods and a strong beat. Spectroscopically observable prominences do not imply photometric CQV-like dips.

The key difference between the prominence and dust clump scenarios is in whether the occulting material of interest is neutral hydrogen, or dust. In the phrasing of the “frozen flux” condition of ideal rigid field magnetohydrodynamics, the tendency of both to become trapped at the corotation radius in the equatorial plane is tied to how of the four relevant forces (gravity, Lorentz, inertial Coriolis, and inertial centrifugal), the Lorentz and Coriolis only act perpendicular to field lines, while gravity and the centrifugal force are in balance at R_{cr} (see Townsend & Owocki 2005, Sec. 2). The magnetic field strength is only relevant in this formulation of the system in that we must have $R_{\text{sonic}} < R_{\text{cr}} < R_{\text{Alfvén}}$ in order for closed loops to exist that can support prominences (Jardine & Collier Cameron 2019). In detail however, the locations of such magnetic fixed points depends on the star’s magnetic field topology (Sanderson et al. 2023).

5.5.1. Gas absorption microphysics

CQVs show broadband flux variations that can be 1-2× deeper in the blue than in the red (Onitsuka et al. 2017; Bouma et al. 2020; Günther et al. 2022; Koen 2023). For neutral hydrogen to produce this effect in absorption, its opacity must be larger in the blue than in the red. Gray (1992) suggests that this might be microphysically possible: while bound-bound absorption provides opacity only at narrow resonant lines, the hydrogen opacity due to bound-free absorption is “jagged” (see Gray 1992, Figure 8.5 and Eq. 8.8), such that at temperatures of $\approx 3,000$ K to $\approx 10,000$ K the observed chromatic transit depths might be reproduced. While bound-free absorption of H^- seems like it might be important at such cool temperatures, in detail this opacity source has the *opposite sign* from what is required to produce deeper dips in the blue than in the red. Thompson scattering is similarly ruled out as a relevant opacity source, because it is gray. The final plausible alternative opacity source is dust, which has the requisite larger absorption cross-section in the blue than the red (Cardelli et al. 1989).

An instructive point of comparison is the rapidly rotating magnetic B star, σ Ori E, which shows dips that are deeper in the blue than in the red (Hesser et al. 1977). Photometric and spectroscopic observations of this star have been understood

in terms of a warped torus of circumstellar material, analogous to the geometries we are discussing for much cooler M dwarfs (Landstreet & Borra 1978; Nakajima 1985; Townsend et al. 2005). This material is unlikely to be dust, due to the relevant sublimation timescales. The opacity is instead thought to be sourced from bound-free absorption from neutral hydrogen (Nakajima 1985), although to our best knowledge direct evidence for this conclusion has yet to be acquired. Separate and smaller-amplitude emission in σ Ori E may also come from electrons scattering photospheric light toward the observer when the clouds are not in transit (Berry et al. 2022).

Given these complexities, it seems important for a future theoretical study to be conducted to determine to what degree the observed chromaticities in CQVs match, or do not match, expectations from radiative transfer. This issue has a key ability to resolve the question of whether the CQVs are explained by dust or by gas, which likely has bearing on whether the material producing the dips is coming from the star, or whether it is a byproduct of the protoplanetary disk.

5.5.2. The lifetime constraint

Independent of the microphysical basis for gas absorption, the observed lifetime of the CQV phenomenon could provide another dimension to discern between the gas vs. dust clump scenarios. Based on the available statistics from e.g. Rebull et al. (2022) and references therein, it seems plausible that CQV occurrence decreases in time, bottoming to zero well before the ≈ 700 Myr age of Praesepe. This is odd in the context of the prominence scenario, because pre-main-sequence M dwarfs spin up over the first $\approx 10^8$ yr; prominences might even be expected to be *more* common at the age of the Pleiades than for younger stars. This broadly assumes that any star that can support prominences will, and that the magnetic topology of rapidly rotating M dwarfs at 100 Myr is similar to that of rapidly rotating M dwarfs at say, 10 Myr. Based on the degree to which M dwarfs remain rapid rotators over the first few gigayears of their lives (e.g. Rebull et al. 2022; Pass et al. 2022), it seems surprising in the gas clump (prominence) scenario that very few stars older than 150 Myr have been seen to exhibit the phenomenon. In the dust clump scenario this is not a problem, because if the dust were externally sourced, it would be expected to have a finite supply.

5.6. Planets or planetesimal swarms near corotation?

Close-in planets are common around M-dwarfs; studies from Kepler have shown that high-mass M dwarfs have ≈ 0.1 planets per star with sizes between $1\text{--}4 R_\oplus$ and orbital periods within 3 days (Dressing & Charbonneau 2015). The number increases to ≈ 0.7 planets per star considering planets out to $P < 10$ days. Extrapolating to all small close-in planets with say $0.1\text{--}4 R_\oplus$ and within 10 days, it is reasonable to expect on average one close-in planet per M dwarf.

In the context of planet formation, the stopping location for the inner-most planet is set by the location of the protoplanetary disk's truncation radius (Izidoro & Raymond 2018). Al-

though this disk truncation radius is defined by equating the magnetic pressure from the stellar magnetosphere with the ram pressure from the inflowing gas, it also tends to coincide with the Keplerian corotation radius for low accretion rates (Hartmann et al. 2016; Li et al. 2022). Within models that have compact multiplanet resonant chains migrating inward due to gas drag, the inner-most planets therefore arrive at $\approx 5\text{--}10$ stellar radii before the disk becomes depleted.

Given this context, it is tempting to try to interpret features of the CQV light curves in terms of the possible presence of either close-in exoplanets or close-in planetesimals. Rocky planets this young could have molten global magma oceans analogous to those that existed on the Earth and Moon (see Lichtenberg et al. 2022), and thus might be undergoing significant outgassing and atmospheric escape. The system would then be analogous to the Jupiter-Io plasma torus (e.g. Neubauer 1980), although with magnetic fields stronger by a factor of $\approx 1,000$. However we emphasize that while this type of configuration seems *a priori* plausible, no direct evidence currently supports it.

One challenge is perhaps that in systems like LP 12-502, the observed dip depth variations would necessarily drive one toward a picture of a disintegrating planetesimal swarm, rather than just a single planetesimal. The need for more than just one launching body would be driven by the observation that we see dips appear and disappear at many different phases, but with roughly the same period. The observed changing dip depths in response to flares would be understood through the planetesimal outflow rates being stalled by changes in the local magnetic field or coronal plasma density. The sizes of these purported planetesimals would need to be $\lesssim 1 R_\oplus$, based on the non-detections of their transits, analogous to e.g. K2-22 (Sanchis-Ojeda et al. 2015) or KOI-2700 (Rappaport et al. 2014). Typical sizes of bodies in the asteroid belt for instance span hundreds of meters to a few kilometers.

There are at least three problems with this concept of a disintegrating planetesimal swarm. First, the model would predict that certain orbital phases would produce recurrent dips if observed over sufficiently long baselines, because the launching planetesimal would be massive enough to remain in orbit, while stochastically ejecting material. An analogous system would be K2-22 (Sanchis-Ojeda et al. 2015). For most CQVs (Figure 4), the data are in tension with this expectation. A second issue is that many of the dips show asymmetries in the wrong direction relative to the naive expectation of a trailing comet tail. Invoking non-exponentially decaying dust distributions as a function of azimuth might be one way out, but such an idea lacks firm theoretical footing. Finally, dynamical stability is a concern: in a model in which any new dip is “explained” by invoking a new planetesimal, one might eventually pack the corotation radius to a degree where instability over short timescales would be guaranteed.

It is certainly possible that exoplanets or exoplanetessimals could end up being connected to the CQV phenomenon, for instance as a possible sources for the occulting dust or gas. However for the time being, none of the CQVs that we have

studied in this work show clear evidence for the nearby planets that we statistically expect should be common.

5.7. From dippers to debris disks

In identifying the two ambiguous CQVs with outlying SEDs (TICs 193136669 and TIC 57830249; Section 3.3), we were prompted to reconsider our light curve-based labeling, and ultimately concluded that these sources are dippers. This episode suggests that there could be overlap between CQVs and dippers. It is also worth emphasizing that our labeling of e.g. TIC 57830249 was based on a single sector of TESS data (Sector 36) when its behavior is relatively periodic and it showed dip depths of a few percent. However in other TESS sectors (e.g. Sector 10), this source looks completely different, varying in apparent flux by a factor of two, with hardly any discernible periodicity at all.

Assessing these results against the backdrop of our increasing understanding of dippers (e.g. Cody et al. 2014; Ansdell et al. 2016; Robinson et al. 2021; Capistrant et al. 2022), it is clear that the loss of an infrared excess is associated with strong changes in a star’s optical variability. It is reasonable to imagine connections between CQVs and dippers: both classes of object can show transient flux dips that are relatively narrow in duration. The dips in both are probably associated with clumps of dust or gas. However the CQV dips are typically more periodic and less deep than those of dippers, and they display far less transience over timescales of a few to tens of cycles. This is probably because CQV stars have demonstrably less dust than (most) dipper stars. At a population level, the CQV stars are also older. A common mystery between the CQVs and dippers, in our own estimation, is how exactly the *narrowness* of the dust clumps is produced. It is not unreasonable to imagine a similar mechanism operating for both types of object, tied perhaps to a shared magnetic topology, or perhaps to a preference for dust to inspiral to the star in clumped structures.

5.8. Are half-cycles important?

The interval of half a cycle period could be significant in the context of CQVs for two reasons. The first is that for material on a circular orbit viewed edge-on, a half-cycle corresponds to the interval between transit and secondary eclipse. The second is that the half-cycle also corresponds to the interval over which half of the star’s surface is visible. Of the CQVs in Figures 3 and 4, a fraction that seems greater than random might exhibit a preference for showing dips or peaks that correspond to the half-cycle interval.

One set of CQVs shows “CQV behavior” (some form of dip complex), but which only lasts for half of any given cycle. TIC 206544316 (Sector 2) is a canonical example; TIC 405910546 (Sector 38), TIC 167664935 (Sector 38), TIC 146539195 (Sector 5), TIC 118449916 (Sector 44), and TIC 312410638 (Sector 38) seem to show the same tendency.

An independent set of CQVs exhibits small dips roughly half a cycle after large dips; it is tempting to label the small dips secondary eclipses. Such sources include TIC 402980664 (Sector 25; relative to the sharpest, deep-

est minimum), TIC 89463560 (Sector 36), TIC 224283342 (Sector 2), and TIC 442571495 (Sector 12).

It is challenging to interpret the significance of such apparent regularities; the objects exhibit such a wide range of variability that for seemingly any “regularity” one might posit, it is easy to come up with counter-example objects which do not follow the trend. In other words, these half-cycle CQVs could simply be a product of the human tendency to pattern match; alternatively, they might yield some important physical significance.

5.9. Mass flux estimate

We can estimate the mass of a transiting cloud by first converting the transit depth to an effective cloud radius, R_{cloud} . For most CQVs in Figure 3, this typically yields $\approx 2\text{-}20 R_{\oplus}$. This size can be converted into a mass estimate by requiring the optical depth τ of the cloud to be at least unity and by positing some composition for the cloud. In other words, a minimum constraint on the number density follows by requiring the cloud to be optically thick. For cases like LP 12-502, this is reasonable because the transit duration implies $R_{\text{cloud}} \ll R_*$. Carrying out the relevant calculation assuming the occulting material is dust grains $1\,\mu\text{m}$ in size, Sanderson et al. (2023) find minimum cloud masses of order $10^{12}\,\text{kg}$ (their Eq. 23), which scale linearly with both the optical depth and dust grain radius. This is comparable to a small asteroid; the asteroid belt itself has a mass of order $\approx 10^{21}\,\text{kg}$ (Park et al. 2019). The previously discussed cool gas prominences would need to have masses of order $10^{14}\,\text{kg}$ (Collier Cameron et al. 1990), about $100\times$ larger than the requisite dust mass.

Our observations provide a direct measurement of how often dips appear and disappear, both due to sudden state-switches, and due to more gradual, secular evolution. For instance, LP 12-502 showed three “state-switch” events over the six months of available TESS observations, during cycles 248-264, 299-315, and 1233-1247. In each case, a dip “turned off”. It is plausible to imagine that these events correspond to either mass being ejected from corotation, or perhaps being accreted onto the star. In either case, the corresponding $\dot{M} \equiv M \cdot dN/dt$ time-averaged over six months is $\approx 3 \times 10^{-18} M_{\odot}\,\text{yr}^{-1} \approx 1 \times 10^{-12} M_{\oplus}\,\text{yr}^{-1}$. Considered cumulatively over the $\approx 10^8$ years for which the CQV phenomenon is observed, this yields a cumulative moved dust mass of $10^{-4} M_{\oplus}$, of order the Solar System’s asteroid belt. If the occulting material is gas, the masses involved would be of order 100 times larger. For cases in which we observe the *growth* of dips, such as the Sector 29 data for TIC 224283342, or Sector 5 of TIC 294328885, the dip depths typically increase by of order a few percent over ten to twenty days. This growth rate yields a mass flux one order of magnitude larger than the earlier estimate.

5.10. Strengthening the magnetic B star connection

Previous work by Stauffer et al. (2017) noted the possible connection between the CQVs and rapidly rotating magnetic B stars such as σ Ori E, which can have circumstellar gas

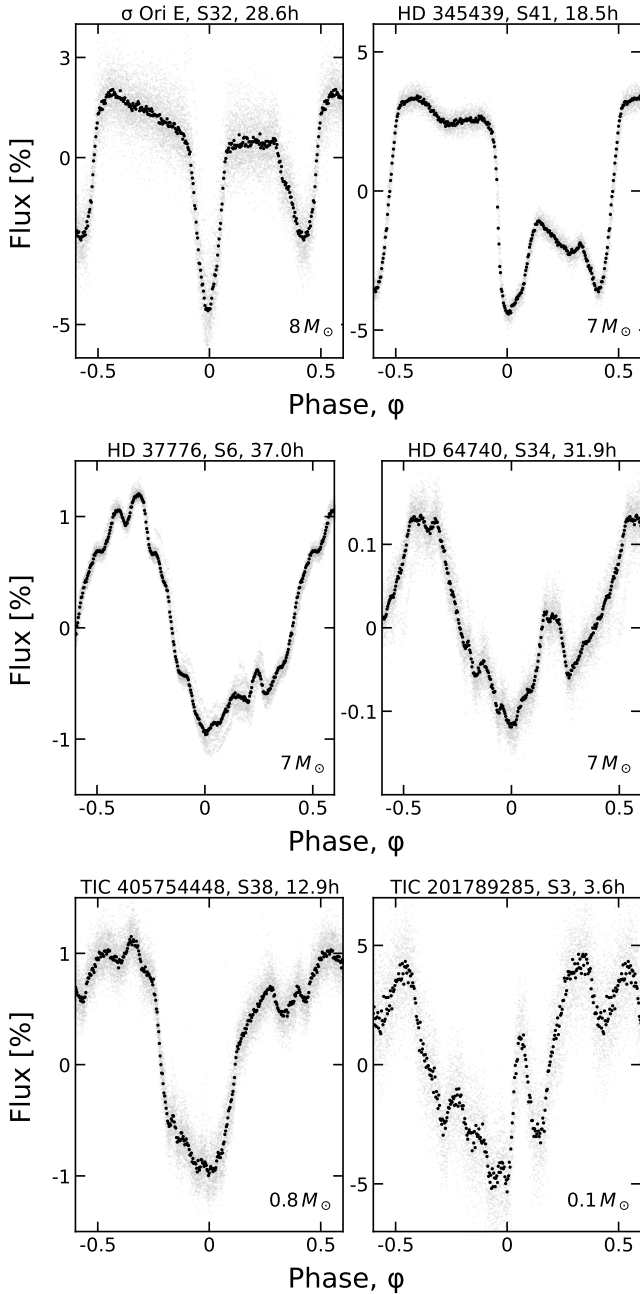


Figure 9. The magnetic B star connection. σ Ori E and HD 345439 (top row) are magnetic B stars with predominantly dipolar magnetic fields known to host circumstellar plasma tori. HD 37776 and HD 64740 (middle row) are analogous magnetic B stars with field topologies dominated by high order multipoles. The bottom row compares the latter systems against the “best-matching” CQV light curves, selected by eye from Figure 3. CQVs have light curves that are visually similar to the topologically complex magnetic B stars. Stellar masses rounded to one significant figure are given in the lower right of each panel; the star, TESS sector, and period are listed in each subtitle.

clouds trapped in corotation (Townsend et al. 2005). The σ Ori class is distinct from Be-star decretion disks, which do not have any obvious connection to the stellar magnetic field (Rivinius et al. 2013).

An argument against the connection between CQVs and the σ Ori E analogs is that the light curve of σ Ori E is much simpler than those in Figure 3, with only two broad local minima, and one “hump” (Townsend et al. 2005; Jayaraman et al. 2022). Within the model proposed by Townsend et al., this is explained by the simplicity of the star’s magnetic field, which to first-order is a dipole, similar to most other magnetic B stars (Aurière et al. 2007; Donati & Landstreet 2009). This approximation matches the qualitative behavior of both the broadband light curves, and the line-profile variations seen in hydrogen, helium, and carbon (Oksala et al. 2012).

Two exceptions to the rule of “simple field topologies for magnetic B stars” are HD 37776 and HD 64740, which are B stars that were previously known from spectropolarimetry to have field geometries dominated by high order multipoles (Kochukhov et al. 2011). Reviewing the literature, we learned that recent TESS light curves of these two B stars appear surprisingly similar to the CQV light curves (Mikulášek et al. 2020). The middle row of Figure 9 shows the phased TESS light curves for these two outlying magnetic B stars, with by-eye “best matching” CQVs shown for comparison. The number of dips per cycle, the shapes of the dips, and the dip depths relative to the sinusoidal envelope, all seem to be quite similar. The implication of this surprising connection is that the highly-structured M dwarf light curves may imply multipolar magnetic fields – since it is the complex fields which are the defining characteristic of these two B stars, relative to other known magnetic B stars like σ Ori E. This is consistent with the non-axisymmetric topologies that have been reported in a small number of M dwarfs for which Zeeman Doppler Imaging is technically feasible (see the review by Kochukhov 2021).

The physical similarity between the B stars and the M dwarfs presumably has its origin in the existence of a “centrifugal magnetosphere” (see Petit et al. 2013). In other words, both classes of objects probably satisfy the condition $R_A > R_{cr}$, for R_A the Alfvén radius. When this condition holds, stable points exist wherever the outward centrifugal force is balanced by the combined effect of gravity and magnetic tension along closed field loops (Nakajima 1985). In the converse “dynamical” case, when $R_A < R_{cr}$, any material launched by the star returns to its surface over the free-fall timescale. A simple order of magnitude estimate assuming a dipole field with $B_0 \approx 1\text{ kG}$ at the star’s surface, a local plasma number density $n \approx 10^9\text{ cm}^{-3}$, and a plasma temperature 10^6 K tends to give Alfvén radii of order a few times the corotation radii, R_{cr} .

6. CONCLUSIONS

In this work, we searched 120-second cadence TESS data collected between July 2018 and Sep 2022 for complex quasiperiodic variables (CQVs). The target stars were 65,760 K and M dwarfs within 150 pc. The selection function was

>80% complete within 30 pc, and <10% complete at distances exceeding 100 pc.

In our target sample, we found 53 objects that showed complex quasiperiodic behavior over at least one TESS sector. These 53 bona fide CQVs are listed in Table 1. This table also includes an additional 14 ambiguous CQVs, whose designation is less certain, and 3 impostors. We inferred ages for all but two of the 70 objects based on association memberships; we also derived temperatures and radii using SED fitting, and then inferred stellar masses by interpolating against stellar evolutionary models. We caution that our selection function was not volume-limited: the TESS 120-second stellar sample had a heterogeneous selection function which may have been biased in favor of young stars over field stars. Previous work however has shown that $\approx 1\text{-}3\%$ of M dwarfs younger than ≈ 100 Myr show the CQV phenomenon (Rebull et al. 2016; Günther et al. 2022).

Analyzing the TESS light curves and stellar properties of our CQVs, we draw the following conclusions.

1. CQVs are quasiperiodic. The mean periods remain fixed over the >1,000-cycle baseline of available observations; but the light curve shapes always evolve (Figure 4).
2. The same CQV can show multiple periods simultaneously. LP 12-502, for instance, showed dips with four distinct periods within $\pm 0.3\%$ of its fundamental period, sometimes simultaneously, and each lasting for up to 50 cycles (Figure 7).
3. CQVs evolve over timescales that are both secular (>100 cycles) and impulsive (<1 cycle). Dip growth seems to happen over durations of at least ten cycles, and slow dip decay can also occur. “State-switches” correspond to dips to collapsing instantaneously, and are almost always linked with observed optical flares. This suggests that the occulting material is sensitive to sudden changes in the magnetic field.
4. The rate of dip evolution can be used to place a model-dependent constraint on how much material is either being accreted or ejected during the state changes (Section 5.9). Order of magnitude estimates require at least an asteroid belt’s worth of dust ($10^{-4} M_{\oplus}$) over 10^8 years, or $\approx 10^{-2} M_{\oplus}$ if the occulting material is gas.
5. The CQV phenomenon persists for $\gtrsim 150$ Myr, based on the existence of multiple CQVs in AB Dor, the Pleiades, and Psc-Eri (Section 2.3). It may even extend to 200 Myr, based on the one CQV we found in the Carina Near moving group (TIC 294328887; ≈ 200 Myr). However the lack of detected CQVs in the Hyades and Praesepe suggests that the lifetime of the phenomenon is limited to the first few hundred million years.
6. The duty cycle for CQVs seems to be $\approx 75\%$, based on the fraction of bona fide CQVs that either turned on or turned off during TESS re-observations, two years after the initial observation.

7. While the majority of detected CQVs have masses of $0.1\text{--}0.5 M_{\odot}$, the upper mass limit for the CQV phenomenon might extend into the K dwarf regime ($<0.8 M_{\odot}$). TIC 405754448 and TIC 405910546, with masses of ≈ 0.8 and $\approx 0.6 M_{\odot}$, are the two massive outliers. However both have peculiarities (Section 5.2.1), and we encourage additional scrutiny of these objects in future work.
8. Surprising analogs to the CQVs exist in magnetic B stars, but only those with multipolar field topologies. Since most magnetic B stars have dipolar magnetic fields, this suggests that the CQV dips and warps are similarly being sculpted by the stellar magnetic fields, and that the magnetic fields themselves are probably also multipolar.
9. The closest CQVs to the Sun are at distances of 15–20 pc, and the brightest have $V \approx 12$ ($J \approx 7.5$). We have found most of them in this work, since our CQV sample was $\gtrsim 80\%$ complete within 30 pc. The lack of CQVs in the volume-complete <15 pc sample of $0.1\text{--}0.3 M_{\odot}$ stars analyzed by Winters et al. (2021) is consistent with this estimate. Expanding our analysis of the TESS data to the full frame images would yield a truly volume-limited selection function, and would expand the CQV census by about a factor of two within 50 pc, and by a factor of ten within 100 pc.

While many questions remain, two in particular will be important for clarifying what these objects might teach us in a broader astrophysical context: 1) Is the eclipsing material responsible for the phenomenon gas or dust? 2) What sets the characteristic clumping size for the circumstellar material?

The distinction between gas or dust is important because it will clarify whether the CQV phenomenon is intrinsic, so that material comes from the star, or extrinsic, so that it is sourced through some generic evolutionary phase of circumstellar disks. This knowledge would in turn propagate to our understanding of whether the phenomenon is primarily teaching us about dust production and processing in circumstellar disks, or whether it is teaching us about the ability of cold gas to remain stable in hot stellar coronae for long durations. Observationally, acquisition of medium- or high-resolution time-series spectra holds the best chance at resolving the gas vs. dust question. Given the observed evolutionary timescales, such data should be acquired simultaneously with photometric time-series observations to help clarify its interpretation.

In both the gas and dust scenarios, CQVs are preferentially viewed edge-on. This implies that after correcting for the line-of-sight inclination, roughly one third of low mass stars (Günther et al. 2022) could trap circumstellar material in the same way. It also suggests that CQVs may preferentially show transiting planets at larger distances than the corotating material, though this may be dependent on whether the magnetic and stellar spin axes tend to be aligned. Given these points, observational follow-up work should include searching for outer transiting planets, and measuring equatorial ve-

locities in order to test whether the stellar inclination angles are indeed preferentially edge-on.

On the theoretical front, building a physical understanding what sets the characteristic size scale of the clumping material would help clarify the nature of the magnetic and plasma environments around these young stars, and would also help build intuition for why the light curves have the bizarre shapes that are observed. The relevant puzzles in plasma physics and radiative transfer could likely be connected to our understanding of the close-in rocky planets that are expected to be present around most of these stars. The challenges intrinsic to both the observational and theoretical work seem worth the effort.

ACKNOWLEDGMENTS

LGB gratefully acknowledges support from the Heising-Simons 51 Pegasi b Fellowship. While many conversations helped encourage this work, a few thank-yous in particular (from LGB) are owed to G. Laughlin, A. Mann, and J. Spake (for a draft version of this paper). This paper relies on data collected by the TESS mission, which are publicly available ([Transactions of the Royal Society A: Mathematical, Physical and Engineering Sciences](#), **370**, 2765). Funding for the TESS mission is provided by NASA's Science Mission Directorate. NIC 402980664 in particular was allocated during the Second Readiness Review to the TESS Guest Investigator programs G022252 (PI: J. Schlieder; Sectors 18, 19, 25, 26) and G04168 (PI: R. Jayaraman; Sector 53).

Astropy Collaboration, Robitaille, T. P., Tollerud, E. J., et al. 2013, *A&A*, **558**, A33

Astropy Collaboration, Price-Whelan, A. M., Sipőcz, B. M., et al. 2018, *AJ*, **156**, 123

Astropy Collaboration, Price-Whelan, A. M., Lim, P. L., et al. 2022, *ApJ*, **935**, 167

Aurière, M., Wade, G. A., Silvester, J., et al. 2007, *A&A*, **475**, 1053

Bailer-Jones, C. A. L., Rybizki, J., Fouesneau, M., Demleitner, M., & Andrae, R. 2021, *AJ*, **161**, 147

Baraffe, I., & Chabrier, G. 2018, *A&A*, **619**, A177

Barber, R. J., Tennyson, J., Harris, G. J., & Tolchenov, R. N. 2006, *MNRAS*, **368**, 1087

Basri, G. 2021, An Introduction to Stellar Magnetic Activity

Bell, C. P. M., Mamajek, E. E., & Naylor, T. 2015, *MNRAS*, **454**, 593

AUTHOR CONTRIBUTION STATEMENTS: PLEASE REVISE IF APPROPRIATE LGB and RJ conceived the project and executed the dip-based and Fourier-based analyses, respectively. SR and RJ vetted the results from the Fourier search. LGB performed the cluster membership, SED, and variability analyses. LR contributed an independent SED analysis, and cross-checked the variability analyses. AD identified the magnetic B star connection. LAH contributed to data analysis and interpretation. GÁB acquired and maintained the servers used to run the dip-finding pipeline. GRR is an architect of the TESS mission. All authors assisted in manuscript writing and revision.

Software: astrobase (Bhatti et al. 2021), astropy (Astropy Collaboration et al. 2013, 2018, 2022), lightkurve (Lightkurve Collaboration et al. 2018), numpy (Harris et al. 2020), pyGAM (Servén & Brummitt 2018), scipy (Virtanen et al. 2020), TESS-point (Burke et al. 2020), wotan (Hippke et al. 2019).

Facilities: *Astrometry*: Gaia (Gaia Collaboration et al. 2018, 2022). *Imaging*: Second Generation Digitized Sky Survey. *Spectroscopy*: Keck:I (HIRES; Vogt et al. 1994). *Photometry*: TESS (Ricker et al. 2015), *Broadband photometry*: 2MASS (Skrutskie et al. 2006), APASS (Henden et al. 2016), Gaia (Gaia Collaboration et al. 2018, 2022), SDSS (York et al. 2000), WISE (Wright et al. 2010).

REFERENCES

- Berry, I. D., Owocki, S. P., Shultz, M. E., & ud-Doula, A. 2022, *MNRAS*, **511**, 4815
- Bhatti, W., Bouma, L., Joshua, et al. 2021, waqasbhatti/astrobase: astrobase v0.5.3, Zenodo
- Bodman, E. H. L., Quillen, A. C., Ansdell, M., et al. 2017, *MNRAS*, **470**, 202
- Bouma, L. G., Winn, J. N., Ricker, G. R., et al. 2020, *AJ*, **160**, 86
- Bouma, L. G., Curtis, J. L., Masuda, K., et al. 2022, *AJ*, **163**, 121
- Boyle, A. W., & Bouma, L. G. 2023, *AJ*, **166**, 14
- Bressan, A., Marigo, P., Girardi, L., et al. 2012, *MNRAS*, **427**, 127
- Brogi, M., Keller, C. U., de Juan Ovelar, M., et al. 2012, *A&A*, **545**, L5
- Burke, C. J., Levine, A., Fausnaugh, M., et al. 2020, TESS-Point: High precision TESS pointing tool, Astrophysics Source Code Library, record ascl:2003.001
- Capistrant, B. K., Soares-Furtado, M., Vanderburg, A., et al. 2022, *ApJS*, **263**, 14
- Cardelli, J. A., Clayton, G. C., & Mathis, J. S. 1989, *ApJ*, **345**, 245
- Chen, Y., Girardi, L., Bressan, A., et al. 2014, *MNRAS*, **444**, 2525
- Christian, S., Vanderburg, A., Becker, J., et al. 2022, *AJ*, **163**, 207
- Cody, A. M., Stauffer, J., Baglin, A., et al. 2014, *AJ*, **147**, 82
- Collier Cameron, A. 1999, in Astronomical Society of the Pacific Conference Series, Vol. 158, Solar and Stellar Activity: Similarities and Differences, ed. C. J. Butler & J. G. Doyle, 146

- Collier Cameron, A., Duncan, D. K., Ehrenfreund, P., et al. 1990, *MNRAS*, 247, 415
- Collier Cameron, A., & Robinson, R. D. 1989, *MNRAS*, 238, 657
- Curtis, J. L., Agüeros, M. A., Mamajek, E. E., Wright, J. T., & Cummings, J. D. 2019, *AJ*, 158, 77
- Dahm, S. E. 2015, *ApJ*, 813, 108
- David, T. J., & Hillenbrand, L. A. 2015, *ApJ*, 804, 146
- Donati, J. F., & Landstreet, J. D. 2009, *ARA&A*, 47, 333
- Dressing, C. D., & Charbonneau, D. 2015, *ApJ*, 807, 45
- Dunstone, N. J., Barnes, J. R., Collier Cameron, A., & Jardine, M. 2006, *MNRAS*, 365, 530
- Fausnaugh, M., Morgan, E., Vanderspek, R., et al. 2021, *PASP*, 133, 095002
- Feiden, G. A. 2016, *A&A*, 593, A99
- Ferreira, J. M. 2000, *MNRAS*, 316, 647
- Gagné, J., Mamajek, E. E., Malo, L., et al. 2018, *ApJ*, 856, 23
- Gaia Collaboration, Brown, A. G. A., Vallenari, A., et al. 2018, *A&A*, 616, A1
- Gaia Collaboration, Vallenari, A., Brown, A. G. A., et al. 2022, *arXiv e-prints*, arXiv:2208.00211
- Gray, D. F. 1992, The observation and analysis of stellar photospheres., Vol. 20
- Gully-Santiago, M. A., Herczeg, G. J., Czekala, I., et al. 2017, *ApJ*, 836, 200
- Günther, M. N., Berardo, D. A., Ducrot, E., et al. 2022, *AJ*, 163, 144
- Harris, C. R., Millman, K. J., van der Walt, S. J., et al. 2020, *Nature*, 585, 357
- Hartmann, L., Herczeg, G., & Calvet, N. 2016, *ARA&A*, 54, 135
- Henden, A. A., Templeton, M., Terrell, D., et al. 2016, VizieR Online Data Catalog, II/336
- Hesser, J. E., Ugarte, P. P., & Moreno, H. 1977, *ApJL*, 216, L31
- Hippke, M., David, T. J., Mulders, G. D., & Heller, R. 2019, *arXiv:1906.00966 [astro-ph]*, arXiv: 1906.00966
- Hippke, M., David, T. J., Mulders, G. D., & Heller, R. 2019, *AJ*, 158, 143
- Izidoro, A., & Raymond, S. N. 2018, in *Handbook of Exoplanets*, ed. H. J. Deeg & J. A. Belmonte, 142
- Jardine, M., & Collier Cameron, A. 2019, *MNRAS*, 482, 2853
- Jayaraman, R., Hubrig, S., Holdsworth, D. L., et al. 2022, *ApJL*, 924, L10
- Jeffries, R. D. 1993, *MNRAS*, 262, 369
- Jenkins, J. M., Twicken, J. D., McCauliff, S., et al. 2016, in *Society of Photo-Optical Instrumentation Engineers (SPIE) Conference Series*, Vol. 9913, Software and Cyberinfrastructure for Astronomy IV, ed. G. Chiozzi & J. C. Guzman, 99133E
- Johns-Krull, C. M., Prato, L., McLane, J. N., et al. 2016, *ApJ*, 830, 15
- Justesen, A. B., & Albrecht, S. 2021, *ApJ*, 912, 123
- Kenyon, S. J., & Hartmann, L. 1995, *ApJS*, 101, 117
- Kerr, R. M. P., Rizzuto, A. C., Kraus, A. L., & Offner, S. S. R. 2021, *ApJ*, 917, 23
- Kochukhov, O. 2021, *A&A Rev*, 29, 1
- Kochukhov, O., Lundin, A., Romanyuk, I., & Kudryavtsev, D. 2011, *ApJ*, 726, 24
- Koen, C. 2021, *MNRAS*, 500, 1366
- . 2023, *MNRAS*, 518, 2921
- Landstreet, J. D., & Borra, E. F. 1978, *ApJL*, 224, L5
- Leitzinger, M., Odert, P., Zaqrashvili, T. V., et al. 2016, *MNRAS*, 463, 965
- Li, R., Chen, Y.-X., & Lin, D. N. C. 2022, *MNRAS*, 510, 5246
- Lichtenberg, T., Schaefer, L. K., Nakajima, M., & Fischer, R. A. 2022, *arXiv e-prints*, arXiv:2203.10023
- Lightkurve Collaboration, Cardoso, J. V. d. M., Hedges, C., et al. 2018, Lightkurve: Kepler and TESS time series analysis in Python, Astrophysics Source Code Library, record ascl:1812.013
- MacLeod, M., & Oklopčić, A. 2022, *ApJ*, 926, 226
- McCann, J., Murray-Clay, R. A., Kratter, K., & Krumholz, M. R. 2019, *ApJ*, 873, 89
- Meingast, S., Alves, J., & Rottensteiner, A. 2021, *A&A*, 645, A84
- Mikulášek, Z., Krtička, J., Shultz, M. E., et al. 2020, in *Stellar Magnetism: A Workshop in Honour of the Career and Contributions of John D. Landstreet*, ed. G. Wade, E. Alecian, D. Bohlender, & A. Sigut, Vol. 11, 46
- Murphy, S. J., Lawson, W. A., & Bessell, M. S. 2013, *MNRAS*, 435, 1325
- Nakajima, R. 1985, *Ap&SS*, 116, 285
- Neubauer, F. M. 1980, *J. Geophys. Res.*, 85, 1171
- Oksala, M. E., Wade, G. A., Townsend, R. H. D., et al. 2012, *MNRAS*, 419, 959
- Onitsuka, M., Fukui, A., Narita, N., et al. 2017, *PASJ*, 69, L2
- Palumbo, E. K., Montet, B. T., Feinstein, A. D., et al. 2022, *ApJ*, 925, 75
- Park, R. S., Vaughan, A. T., Konopliv, A. S., et al. 2019, *Icarus*, 319, 812
- Pass, E. K., Charbonneau, D., Irwin, J. M., & Winters, J. G. 2022, *ApJ*, 936, 109
- Pecaut, M. J., & Mamajek, E. E. 2016, *MNRAS*, 461, 794
- Petit, V., Owocki, S. P., Wade, G. A., et al. 2013, *MNRAS*, 429, 398
- Popinchalk, M., Faherty, J. K., Curtis, J. L., et al. 2023, *ApJ*, 945, 114
- Pribulla, T., Borkovits, T., Jayaraman, R., et al. 2023, *MNRAS*, 524, 4220
- Rajpurohit, A. S., Reylé, C., Allard, F., et al. 2013, *A&A*, 556, A15
- Rappaport, S., Barclay, T., DeVore, J., et al. 2014, *ApJ*, 784, 40
- Rappaport, S., Levine, A., Chiang, E., et al. 2012, *ApJ*, 752, 1
- Ratzenböck, S., Meingast, S., Alves, J., Möller, T., & Bomze, I. 2020, *A&A*, 639, A64

- Rebull, L. M., Stauffer, J. R., Cody, A. M., et al. 2018, *AJ*, **155**, 196
- Rebull, L. M., Stauffer, J. R., Hillenbrand, L. A., et al. 2022, *AJ*, **164**, 80
- Rebull, L. M., Stauffer, J. R., Bouvier, J., et al. 2016, *AJ*, **152**, 114
- Reiners, A., & Basri, G. 2009, *A&A*, **496**, 787
- Ricker, G. R., Winn, J. N., Vanderspek, R., et al. 2015, *Journal of Astronomical Telescopes, Instruments, and Systems*, **1**, 014003
- Rivinius, T., Carciofi, A. C., & Martayan, C. 2013, *A&A Rev*, **21**, 69
- Robinson, C. E., Espaillat, C. C., & Owen, J. E. 2021, *ApJ*, **908**, 16
- Rodriguez, D. R., van der Plas, G., Kastner, J. H., et al. 2015, *A&A*, **582**, L5
- Sanchis-Ojeda, R., Rappaport, S., Pallè, E., et al. 2015, *ApJ*, **812**, 112
- Sanderson, H., Jardine, M., Collier Cameron, A., Morin, J., & Donati, J. F. 2023, *MNRAS*, **518**, 4734
- Servén, D., & Brummitt, C. 2018, pyGAM: Generalized Additive Models in Python
- Skrutskie, M. F., Cutri, R. M., Stiening, R., et al. 2006, *AJ*, **131**, 1163
- Somers, G., Cao, L., & Pinsonneault, M. H. 2020, *ApJ*, **891**, 29
- Speagle, J. S. 2020, *MNRAS*, **493**, 3132
- Stassun, K. G., Kratter, K. M., Scholz, A., & Dupuy, T. J. 2012, *ApJ*, **756**, 47
- Stassun, K. G., Oelkers, R. J., Pepper, J., et al. 2018, *AJ*, **156**, 102
- Stauffer, J., Collier Cameron, A., Jardine, M., et al. 2017, *AJ*, **153**, 152
- Stauffer, J., Rebull, L., David, T. J., et al. 2018, *AJ*, **155**, 63
- Stellingwerf, R. F. 1978, *ApJ*, **224**, 953
- Townsend, R. H. D., & Owocki, S. P. 2005, *MNRAS*, **357**, 251
- Townsend, R. H. D., Owocki, S. P., & Groote, D. 2005, *ApJL*, **630**, L81
- Vanderburg, A., Johnson, J. A., Rappaport, S., et al. 2015, *Nature*, **526**, 546
- Vial, J.-C., & Engvold, O. 2015, *Astrophysics and Space Science Library*, Vol. 415, Solar Prominences
- Vines, J. I., & Jenkins, J. S. 2022, *MNRAS*, **513**, 2719
- Virtanen, P., Gommers, R., Oliphant, T. E., et al. 2020, *Nature Methods*, **17**, 261
- Vogt, S. S., Allen, S. L., Bigelow, B. C., et al. 1994, in *Society of Photo-Optical Instrumentation Engineers (SPIE) Conference Series*, Vol. 2198, *Instrumentation in Astronomy VIII*, ed. D. L. Crawford & E. R. Craine, 362
- Vos, J. M., Faherty, J. K., Gagné, J., et al. 2022, *ApJ*, **924**, 68
- Waugh, R. F. P., & Jardine, M. M. 2022, *MNRAS*, **514**, 5465
- Winn, J. N. 2010, in *Exoplanets*, ed. S. Seager, 55
- Winters, J. G., Charbonneau, D., Henry, T. J., et al. 2021, *AJ*, **161**, 63
- Wright, E. L., Eisenhardt, P. R. M., Mainzer, A. K., et al. 2010, *AJ*, **140**, 1868
- York, D. G., Adelman, J., Anderson, John E., J., et al. 2000, *AJ*, **120**, 1579
- Zhan, Z., Günther, M. N., Rappaport, S., et al. 2019, *ApJ*, **876**, 127
- Zieba, S., Zwintz, K., Kenworthy, M. A., & Kennedy, G. M. 2019, *A&A*, **625**, L13
- Zuckerman, B. 2019, *ApJ*, **870**, 27
- Zuckerman, B., Bessell, M. S., Song, I., & Kim, S. 2006, *ApJL*, **649**, L115

Table 1. Bonafide, candidate, and debunked complex quasiperiodic variables from the TESS 2-minute data. **For internal review, full versions are available here** <https://www.dropbox.com/scl/fo/twn4s9ckbevf75jqhtoy1/h?rlkey=t5cn8cx2uoc2ptdm9e570kp1b&dl=0>

TIC	<i>T</i>	<i>d</i>	$G_{\text{BP}} - G_{\text{RP}}$	RUWE	<i>P</i>	Assoc	Age	T_{eff}	R_{\star}	M_{\star}	R_{cr}	Quality	N_{sector}
–	mag	pc	mag	–	hr	–	Myr	K	R_{\odot}	M_{\odot}	R_{\star}	–	–
368129164	9.29	18.3	2.9	6.95	6.44	ABDMG	149	3140	0.71	0.4	1.81	1	3
405754448	9.63	96.5	1.75	4.66	12.92	LCC	15	4273	1.5	0.82	1.74	1	5
167664935	10.31	63.0	2.52	1.62	14.05	UCL	16	3325	1.42	0.38	1.5	1	3
311092148	11.03	26.9	3.04	1.31	7.86	COL	42	3035	0.5	0.27	2.6	1	1
402980664	11.11	21.3	3.05	1.26	18.56	COL	42	3080	0.37	0.22	5.76	1	10
50745567	11.28	38.5	3.23	1.84	6.34	BPMG	24	3014	0.67	0.28	1.68	1	2
425933644	11.4	44.3	2.83	2.29	11.67	THA	45	3151	0.63	0.4	3.06	1	6
142173958	11.61	72.6	3.1	1.43	11.76	TWA	10	3028	1.15	0.26	1.45	1	3
146539195	11.62	48.6	3.38	1.59	6.73	BPMG	24	2898	0.8	0.24	1.38	1	2
206544316	11.63	43.1	2.89	1.27	7.73	THA	45	3114	0.57	0.35	2.44	1	6
335598085	11.9	105.9	2.86	1.64	15.85	LCC	15	3119	1.34	0.28	1.56	1	3
405910546	12.11	112.2	2.36	1.09	37.99	LCC	15	3455	0.92	0.6	5.26	1	4
272248916	12.15	80.3	2.84	3.18	8.9	UCL	16	3193	0.81	0.4	1.97	1	3
178155030	12.17	46.8	2.91	1.23	11.67	THA	45	3097	0.49	0.3	3.53	1	4
224283342	12.29	38.1	3.04	1.24	21.3	COL	42	3050	0.39	0.22	6.08	1	3
89026133	12.31	139.2	2.82	2.4	11.2	UCL	16	3188	1.33	0.31	1.29	1	3
234295610	12.51	48.2	3.05	1.13	18.29	THA	45	3074	0.44	0.27	5.09	1	3
118449916	12.54	69.2	3.1	8.17	12.31	TAU	2	3025	1.04	0.28	1.7	1	4
67897871	12.55	145.5	3.02	1.67	6.23	USCO	10	3082	1.5	0.18	0.65	1	2
353730181	12.65	107.3	2.75	1.17	13.51	TAU	2	3253	0.8	0.41	2.65	1	4
201898222	12.68	42.2	3.22	1.14	10.7	THA	45	2996	0.39	0.2	3.69	1	5
264767454	12.73	112.6	2.93	16.58	10.01	COL	42	3150	1.0	0.42	1.76	1	13
442571495	12.75	78.5	3.03	1.38	9.59	UCL	16	3099	0.65	0.3	2.35	1	3
2234692	12.8	53.6	3.0	1.08	6.52	COL	42	3098	0.44	0.26	2.56	1	7
94088626	12.88	57.8	3.06	1.1	6.6	ARG	45	3090	0.46	0.27	2.53	1	2
264599508	12.88	80.0	3.0	1.53	7.9	COL	42	3098	0.62	0.4	2.4	1	7
363963079	12.92	81.8	3.1	5.57	7.82	ARG	45	3040	0.67	0.4	2.21	1	7
193831684	13.03	51.5	3.2	1.06	31.02	BPMG	24	2971	0.42	0.2	6.87	1	3
177309964	13.1	91.1	2.93	1.31	10.88	CAR	45	3125	0.62	0.4	2.95	1	34
425937691	13.18	43.8	3.79	1.69	4.82	THA	45	2782	0.41	0.16	1.91	1	5
141146667	13.28	57.5	3.29	1.18	3.93	FIELD	NaN	2968	0.42	NaN	NaN	1	6
332517282	13.29	39.1	3.29	0.93	9.67	ABDMG	149	2975	0.28	0.2	4.87	1	3
144486786	13.3	70.4	3.07	7.62	6.82	COL	42	3074	0.51	0.3	2.38	1	4
38820496	13.3	44.1	3.38	1.21	15.73	THA	45	2903	0.34	0.16	5.13	1	5
289840926	13.31	40.2	3.76	1.0	4.8	BPMG	24	2807	0.36	0.14	2.05	1	3
404144841	13.33	76.0	3.2	1.03	10.74	TWA	10	3008	0.52	0.22	2.86	1	4
89463560	13.45	126.9	2.97	1.31	9.43	ARG	45	3055	0.75	0.37	2.15	1	10
300651846	13.49	109.6	2.87	1.25	8.26	CAR	45	3136	0.62	0.4	2.44	1	31
267953787	13.49	130.6	3.58	1.09	17.46	TAU	2	2826	1.06	0.12	1.59	1	4
58084670	13.58	140.6	2.81	1.04	11.16	FIELD	NaN	3138	0.77	NaN	NaN	1	6
68812630	13.6	132.7	3.24	1.24	9.04	TAU	2	2996	0.76	0.27	1.86	1	3
141306513	13.65	50.0	3.42	1.23	13.36	THA	45	2964	0.32	0.16	4.85	1	2
5714469	13.73	78.4	3.66	1.07	10.35	UCL	16	2828	0.54	0.18	2.53	1	3

Table 1 *continued*

Table 1 (*continued*)

201789285	14.03	45.2	3.85	1.18	3.64	THA	45	2757	0.3	0.12	2.02	1	5
294328887	14.23	97.8	3.23	1.11	8.51	CARN	200	2994	0.45	0.35	3.33	1	35
302160226	14.24	147.6	3.07	1.16	7.88	APER	86	3065	0.62	0.4	2.4	1	2
312410638	14.3	138.8	3.14	1.11	28.06	UCL	16	3030	0.58	0.25	5.11	1	3
251496897	14.36	115.0	3.0	1.11	8.38	ARG	45	3100	0.44	0.27	3.04	1	2
38539720	14.52	132.1	3.38	1.27	9.16	PERI	120	2924	0.57	0.25	2.43	1	1
359892714	14.53	94.0	3.99	1.18	11.33	EPSC	3	2675	0.55	0.13	2.36	1	6
118769116	14.58	120.3	3.6	1.11	8.56	TAU	2	2852	0.56	0.2	2.18	1	4
440725886	14.69	131.6	2.94	1.23	3.92	PLE	112	3109	0.45	0.35	1.99	1	5
397791443	15.01	149.5	3.07	1.05	6.95	LCC	15	3031	0.48	0.22	2.32	1	6
160329609	9.65	8.7	3.41	1.28	24.31	ARG	45	2912	0.35	0.16	6.6	0	3
59836633	11.38	62.1	2.72	1.18	14.96	BPMG	24	3282	0.82	0.48	2.91	0	3
148646689	12.14	142.4	2.44	2.24	10.63	UCL	16	3466	1.25	0.55	1.61	0	3
280945693	12.27	98.3	2.97	1.1	15.27	LCC	15	3103	1.09	0.31	1.94	0	5
149838027	12.28	44.2	3.07	1.33	12.89	THA	45	3051	0.46	0.26	3.83	0	3
165184400	12.37	43.1	3.03	1.14	15.91	THA	45	3076	0.42	0.25	4.74	0	4
245834739	12.55	110.5	2.85	1.25	10.47	TAU	2	3112	1.02	0.36	1.68	0	6
125843782	13.01	128.5	2.87	0.99	44.17	TAU	2	3135	0.9	0.35	4.97	0	4
244161191	13.17	44.4	3.54	1.33	7.17	COL	42	2860	0.38	0.18	2.8	0	3
231058925	13.17	51.1	3.26	1.15	8.87	THA	45	2978	0.38	0.2	3.33	0	5
245874053	13.26	142.2	3.2	1.18	25.98	TAU	2	3017	1.16	0.26	2.45	0	4
301676454	13.4	71.1	3.07	1.35	9.18	ARG	45	3009	0.47	0.25	2.96	0	1
67745212	13.63	27.7	3.82	1.09	5.12	COL	42	2781	0.21	0.09	3.17	0	2
259586708	13.82	96.3	2.93	1.22	22.52	COL	42	3133	0.46	0.29	5.84	0	7
435903839	11.95	92.4	2.48	11.63	10.82	ABDMG	149	3458	0.76	0.54	2.66	-1	6
57830249	11.96	48.7	3.21	1.27	43.82	TWA	10	2948	0.7	0.25	5.63	-1	3
193136669	13.06	61.3	3.51	1.08	37.64	TWA	10	2855	0.58	0.19	5.62	-1	4

NOTE—This table includes 53 CQVs (Quality flag 1), 14 ambiguous CQVs (Quality flag 0), and 3 impostors (Quality flag -1). The machine-readable version, available online, includes additional columns for the Gaia DR2 source identifiers and parameter uncertainties. The age uncertainties are typically $\approx \pm 10\%$, but can be asymmetric. **The median temperature, radius, and mass uncertainties are $\pm XXX$ K, $\pm XX\%$, and $\pm YY\%$ respectively.** N_{sector} denotes the number of TESS sectors for which data are expected to be acquired between July 2018 and Oct 2024. Association names and provenance follow conventions adopted by Gagné et al. (2018): ABDMG: AB Doradus moving group (Bell et al. 2015). ARG: Argus (Zuckerman 2019). APER: α Persei open cluster (Boyle & Bouma 2023). BPMG: β Pic moving group (Bell et al. 2015). CARN: Carina Near moving group (Zuckerman et al. 2006). COL: Columba (Bell et al. 2015). EPSC: ϵ Chamaeleontis (Murphy et al. 2013). LCC: Lower Centaurus Crux (Pecaut & Mamajek 2016). PERI: Pisces-Eridani (Curtis et al. 2019). PLE: Pleiades (Dahm 2015). TAU: Taurus (Kenyon & Hartmann 1995). THA: Tucana-Horologium association (Bell et al. 2015). TWA: TW Hydriæ association (Bell et al. 2015). UCL: Upper Centaurus Lupus (Pecaut & Mamajek 2016). USCO: Upper Scorpious (Pecaut & Mamajek 2016).

APPENDIX

A. TIC 300651846

Figures 10 and 11 show 120-second cadence data for TIC 300651846, a CQV in the TESS continuous viewing zone. If it were not for the existence of TIC 402980664, this source would probably have received greater attention. With the exception of a few sectors, TESS data will exist for TIC 300651846 for at least Sectors 1-12, 27-39, and 61-69. While most of the available data will exist in the full frame images, in Figures 10 and 11 focus only on the currently available 120-second cadence data.

During Sectors 32-39, the source shows between one and four local minima per cycle. During the early portions of Sectors 61-65, it is somewhat more complex, with at least five clear local minima per cycle. As the source evolves, this complexity decreases, while the sharpness of one of the minima appears to increase. We did not find evidence for any obvious “state-switches” analogous to those that we observed in LP 12-502; gradual evolution over timescales of ≈ 50 -100 cycles seem to be the norm for TIC 300651846. Unlike the TIC 402980664 river plots (Figure 7), we did not subtract any “continuum sinusoid” for this source, because the continuum is not as obviously defined.

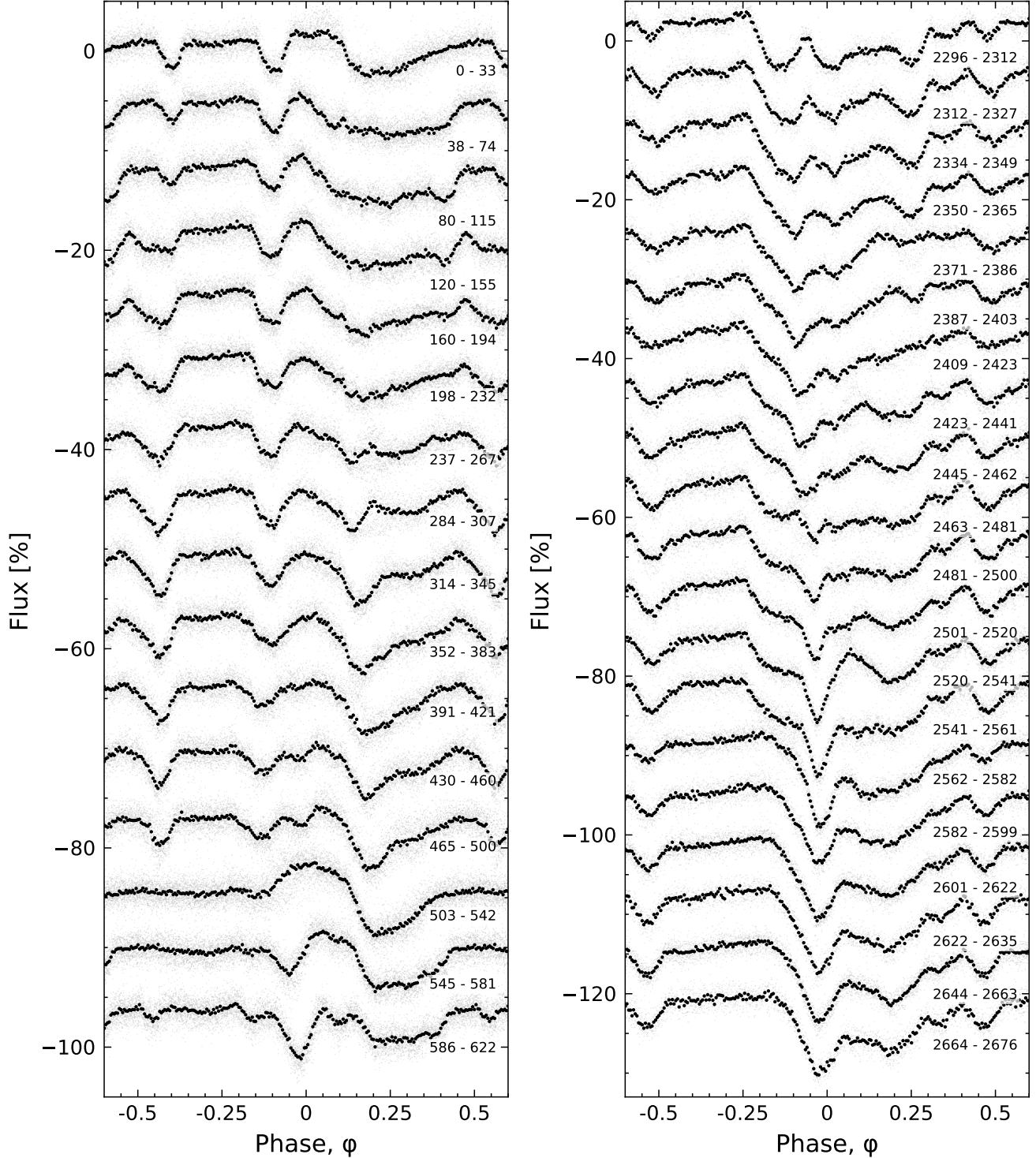


Figure 10. Light curve evolution of TIC 300651846. All available 120-second cadence data as of 2023 Aug 11 are shown. Cycles 0 to 622 span TESS Sectors 32-39 (Nov 2020–June 2021); cycles 2296-2676 span Sectors 61-65 (Jan–June 2023). We assumed a 8.254 hr period and a fixed reference epoch (BTJD 2174.127) for both panels. Light curve segments are split based on the presence of gaps longer than three hours. Cycle numbers are listed in the lower-right of each light curve segment.

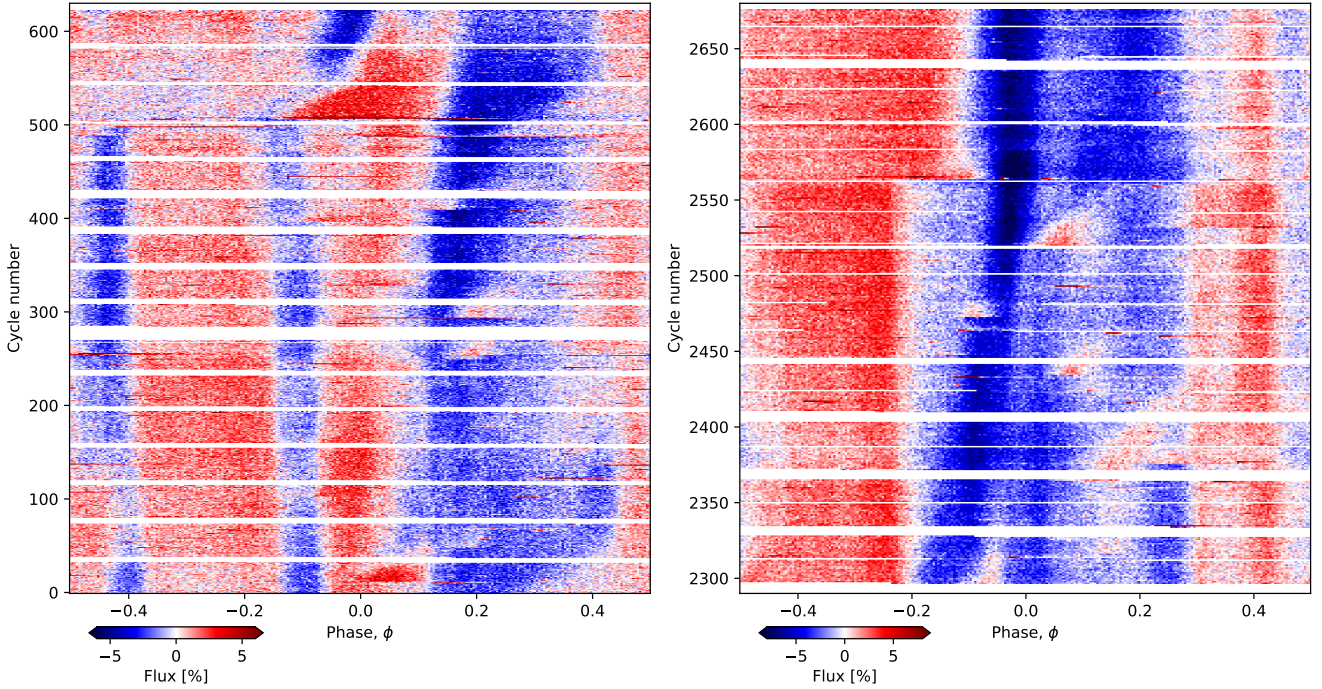


Figure 11. River plots of TIC 300651846. This is an alternative visualization of the data in Figure 10. All available 120-second cadence data as of 2023 Aug 11 are shown. Cycles 0 to 622 span TESS Sectors 32-39 (Nov 2020–June 2021); cycles 2296-2676 span Sectors 61-65 (Jan–June 2023). We assumed $P=8.254$ hr and $t_0=2174.127$ [BTJD]. Note that the two panels have slightly different color scales.

B. NO SIGNIFICANT POWER AT 20 SECOND CADENCE

TESS was the first instrument to show that CQV light curves contain power at timescales of a few minutes (Zieba et al. 2019; Günther et al. 2022). This advance was enabled by the fifteen-fold faster cadence in the TESS 2-minute data, relative to K2. A logical follow-up is to ask whether the periodic components of the CQV light curves contain power at timescales below one minute. Between 2020 and 2021, we observed 10 CQVs at 20-second cadence with TESS in order to explore this question (TESS DDT029). The stars were TICs 142173958, 146539195, 24518895, 276453848, 264599508, 363963079, 144486786, 408188366, 300651846, 262400835. These sources were selected from CQVs known at the time to have short periods and sharp features when observed at 2-minute cadence. Comparing the 20-second to 120-second data for these stars (data available on MAST), we concluded that these CQVs did not contain appreciable power at timescales shorter than a few minutes.